OULU 2007
C 276

ACTA UNIVERSITATIS OULUENSIS

Géza Tóth

COMPUTER MODELING SUPPORTED FABRICATION PROCESSES FOR ELECTRONICS APPLICATIONS

FACULTY OF TECHNOLOGY,
DEPARTMENT OF ELECTRICAL AND INFORMATION ENGINEERING,
UNIVERSITY OF OULU

ACTA UNIVERSITATIS OULUENSIS
C Technica 276

GÉZA TÓTH

COMPUTER MODELING SUPPORTED FABRICATION PROCESSES FOR ELECTRONICS APPLICATIONS

Academic dissertation to be presented, with the assent of the Faculty of Technology of the University of Oulu, for public defence in Auditorium IT116, Linnanmaa, on May 25th, 2007, at 12 noon

OULUN YLIOPISTO, OULU 2007

Acta Univ. Oul. C 276, 2007

Supervised by
Professor Jouko Vähäkangas

Reviewed by
Professor Matti Alatalo
Professor Jaakko Lenkkeri

ISBN 978-951-42-8470-0 (Paperback)
ISBN 978-951-42-8471-7 (PDF)
http://herkules.oulu.fi/isbn9789514284717/
ISSN 0355-3213 (Printed)
ISSN 1796-2226 (Online)
http://herkules.oulu.fi/issn03553213/

Cover design
Raimo Ahonen

OULU UNIVERSITY PRESS
OULU 2007

Tóth, Géza, Computer modeling supported fabrication processes for electronics applications
Faculty of Technology, University of Oulu, P.O.Box 4000, FI-90014 University of Oulu, Finland, Department of Electrical and Information Engineering, University of Oulu, P.O.Box 4500, FI-90014 University of Oulu, Finland
Acta Univ. Oul. C 276, 2007
Oulu, Finland

Abstract

The main objective of this thesis is to study unique cases for computer-assisted finite element modeling (FEM) of thermal, mechanical and thermo-mechanical problems related to silicon and carbon. Computational modeling contributed to solve scientific problems either by validating the experimental results obtained earlier or by predicting the behavior of a particular system. In the model generation phase, emphasis is placed on simplification of a physical problem without loosing the validity or important details. As a consequence of reasonably reduced variables and also degrees of freedom of the elements in our models, the simulations could be performed using a commercial FEM software package, ANSYS®.

To test the capabilities of the method (i) a steady-state finite element thermal analysis has been accomplished and verified by experiments for the case of laser-assisted heating of different materials. (ii) Mechanisms (Dember and Seebeck effects) responsible for the reduction of gold ions and deposition of metallic gold on p-type semiconductors from liquid precursors have been investigated by computing the surface temperature profiles of silicon wafers exposed to laser irradiation. (iii) Temperature field in a multi-component system caused by laser illumination was modeled to determine the heat affected zone in the case of laser soldering of flip-chips on transparent printed circuit board assemblies. (iv) Origin of the experimentally observed residual strain in thermally oxidized porous silicon structures was revealed by computing the strain fields in silicon-silicon oxide porous materials considering both intrinsic and thermal stress components. (v) Finally, we demonstrated that Joule heat generated on a silicon chip can be removed efficiently using micro-fin structures made from aligned carbon nanotubes. Computational fluid dynamics and thermal-electric finite element models were developed to study the steady-state laminar coolant flow and also the temperature distribution for the chips.

The presented novel results have potential in silicon and carbon nanotube based technologies, including deeper understanding of the processes and problems in manufacturing electronic devices.

Keywords: carbon nanotubes, finite element modeling, porous silicon, silicon

Acknowledgements

First of all, I wish to thank my supervisor Professor Jouko Vähäkangas for his support and help during my studies and research work. I would like to express my greatest gratitude and respect to Dr. Krisztán Kordás, the tutor of my studies, for his encouragement, help and friendship.

I also wish to thank for the support and for the grateful discussions to Docent Antti Uusimäki, Emeritus Professor Seppo Leppävuori, also to Dr. Robert Vajtai and Professor Pulickel M. Ajayan (Department of Materials Science & Engineering and Rensselaer Nanotechnology Center, Rensselaer Polytechnic Institute, Troy, USA), Professor László Nánai (Department of Physics, Juhász Gyula Teacher Training Faculty, University of Szeged, Szeged, Hungary), Dr. Andrea Edit Pap (Research Institute for Technical Physics and Materials Science of the Hungarian Academy of Sciences, Budapest, Hungary) and to Professor Thomas F. George (University of Missouri, St. Louis, USA). I also want acknowledge everyone from the Microelectronics and Materials Physics Laboratories for their contribution to my research work and for the great working atmosphere.

I would like to thank Professor Matti Alatalo and Professor Jaakko Lenkkeri for reviewing and commenting on my thesis.

This work has been accomplished at the Microelectronics and Materials Physics Laboratories during the years 2004-2007. The work was financially supported by the Academy of Finland, Tauno Tönning Foundation and Nokia Scholarship, which are gratefully acknowledged.

Special thanks are expressed to my friends in Oulu and in Hungary, my former mentors and teachers in Hungary, to my loving mother and my father who encouraged me during the long years of study. Finally, my deepest gratitude to my amazing wife, for the continuous support, loving and caring.

Thank you all!

Oulu, April 2007 Géza Tóth

List of original publications

This thesis is based on a book chapter and four journal papers, which are cited in the text by their Roman numerals.

I Kordás K, Tóth G, Remes J, Nánai L & Szatmári S (2005) Current trends in depositing and patterning metal films. In: Popescu M (ed) Optoelectronic Materials and Devices Volume 2, INOE, Romania: 239-263.

II Tóth G, Kordás K, Vähäkangas J, Uusimäki A, Leppävuori S, George TF & Nánai L (2005) Laser-induced gold deposition on p+-Si from liquid precursors: A Study on the reduction of gold ions through competing Dember and Seebeck effects. Journal of Physical Chemistry B 109(15): 6925-6928.

III Kordás K, Pap AE, Tóth G, Pudas M, Jääskeläinen J, Uusimäki A, Leppävuori S & Vähäkangas J (2006) Laser soldering of flip-chips. Optics and Lasers in Engineering 44(2): 112-121.

IV Tóth G, Kordás K, Pap AE, Vähäkangas J, Uusimäki A & Leppävuori S (2005) Origin and FEM-assisted evaluation of residual stress in thermally oxidized porous silicon. Computational Materials Science 34(2): 123-128.

V Kordás K, Tóth G, Moilanen P, Kumpumäki M, Vähäkangas J, Uusimäki A, Vajtai R & Ajayan PM (2007) Chip cooling with integrated carbon nanotube microfin architectures. Applied Physics Letters 90(12): 123105 1-3.

The research work of this thesis is divided into three parts. In the first one, temperature fields caused by Gaussian laser beam illumination are investigated in various systems to solve problems related to heat-transfer problem in both isotropic and anisotropic materials (I), to reveal surface temperature profiles of silicon surfaces heated with a focused laser beam and in turn explain the laser induced chemical reduction of gold ions to gold metal on p-type semiconductor surfaces (II) and to study the heat affected zone in a novel laser soldering process of flip-chips on transparent printed circuit boards (III).

In the second part, a thermo-mechanical finite element model is constructed to analyze the origin of residual strain in thermally oxidized porous silicon structures (IV).

Finally, we demonstrate and investigate chip cooling with micro-fined structures of aligned carbon nanotube films mounted on flip-chips. Computational fluid dynamics (CFD) and thermal-electric finite element models were developed to study the steady-state laminar coolant flow and also the temperature distribution for the chips (V).

All the finite element simulations and most of the theoretical considerations were accomplished by the author of this thesis. In publication II all, and in

publication V (including carbon nanotube synthesis) significant amount of the experimental work was carried out by the author. The rest of the experimental work and the corresponding calculations were done in collaboration with the co-authors. Publications II and III were solely and a significant part of publication I (book chapter) was written by the author. The other publications were co-written by the author.

The experimental and computational work was executed at the Microelectronics and Materials Physics Laboratories, Department of Electrical and Information Engineering, University of Oulu. Field emission scanning electron microscopy (FESEM), transmission electron microscopy (TEM) and energy dispersive X-ray (EDX) analysis and some parts of X-ray diffraction (XRD) analyses were accomplished by the author in the Institute of Electron Optics, University of Oulu.

Contents

1 Introduction

"The supreme goal of all theory is to make the irreducible basic elements as simple and as few as possible without having to surrender the adequate representation of a single datum of experience."

Albert Einstein, 1933

1.1 Computer-assisted solutions in materials science

Materials science is a collective term standing for the investigation of materials structure, properties, processing and their conjunction with each others. Materials science deals with structural details and related phenomena on the atomic scale but also with the macroscopic behavior of large scale objects and components. It is an explicitly multidisciplinary field involving applied physics, chemistry, biology, mechanical and electrical engineering as well as nanoscience and nanotechnology to study and implement many different types of materials such as metals and alloys, semi- and superconductors, ceramics, glasses, and their composites towards novel applications.

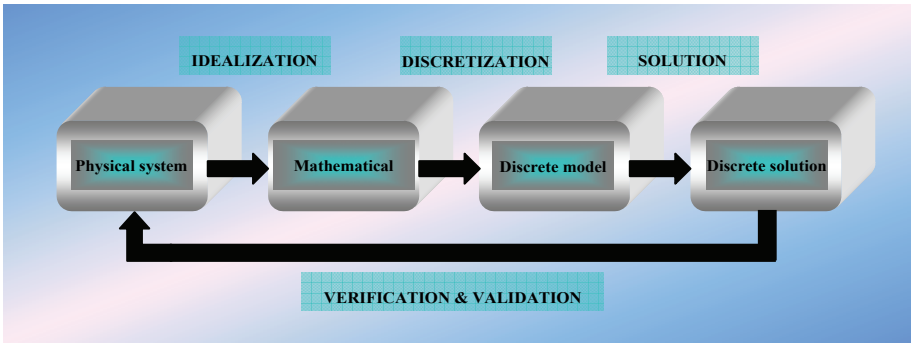

Fig. 1. Simplified view of the physical simulation process (Carlos 2004).

To explain physical systems - comprising of matter and energy - we need to create a model (idealization), together with a mathematical formulation, using the axioms and laws of physics. Since most physical systems tend to be highly complex, there is usually a need for a simplified but valid model as a conceptual representation of the particular problem. Mathematical modeling is an abstraction tool by which complexity can be reduced. This is achieved by disregarding physical details that are not relevant to the analyzing process. For example, a

continuum material model essentially ignores crystal, molecular and atomic levels of matter; simply by using effective or averaged materials parameters that provide a sufficient description of interactions on macro scale (unless we want to gain information on molecular or sub-atomic level). Even if we apply models of physical systems with effective materials properties, the solution of related equations is not straightforward, since those usually involve sets of coupled partial differential equations in space and time with corresponding boundary and/or interface conditions. Such analytical models have too large number of degrees of freedom to enable analytical solutions (those are typically restricted to regular geometries and simple boundary conditions) or doing so would require a tremendous effort and computing power. The practical way out is accomplished by numerical simulation (Fig. 1). To make numerical simulations reasonable, it is necessary to reduce the number of degrees of freedom to a convincingly low finite number. The reduction is called discretization, which is extended to both space and time dimensions. There are two common classes of discretization techniques: finite difference and finite element methods (FEM). With finite difference methods, a differential equation is written for each node, and the derivatives are replaced by difference equations. This approach results in a set of coupled linear equations. Although finite difference methods are easy to understand and utilize in simple problems, difficulties might arise, when complex geometries, boundary conditions or anisotropic materials parameters are involved. The finite element method uses integral formulations to create a system of algebraic equations. An approximate continuous function is assumed to represent the solution for each element having a certain number of nodes and degrees of freedom. The complete solution is then generated by connecting or assembling the individual solutions, allowing continuity at the inter-elemental boundaries.

The first calculations that were related to the finite element method are dated back to the end of 19th century. In 1873 Alberto Castigliano presented his dissertation "Intorno ai sistemi elastici" on a theorem for computing displacement as partial derivative of strain energy. This theorem includes the method of least-work as a special case. John W. Strutt's (Lord Rayleigh) study on "The theory of sound" published in 1877-1878 established a method of calculating approximate natural frequencies for vibrating mechanical and electrical system assuming a deflected shape and balancing kinetic and strain energies. A few years later Walter Ritz applied variational methods for the clamped plate problem "Über eine neue methode zur lösung gewisser variationsproblem der mathematischen physik". In 1915 Boris G. Galerkin published an article "Series solution of some problems in

elastic equilibrium of rods and plates", in which he put forward a method for finding the approximate solution of an operator equation in the form of a linear combination of the elements of a given linearly independent system. Stephan P. Timoshenko (1878-1972) published his paper "On the correction for shear of the differential equation for transverse vibration of prismatic bars". He used a mathematical model to describe the transverse vibration of beams. The model was presented in the context of vibration and dynamics. Hans J. Reissner (1874-1967) designed the first successful aircraft with all-metal wing and tail surfaces and the first controllable-pitch propeller with the use of turbulence and aerodynamic wing theory in the 1940's. The first application of "finite element method" as a numerical method was given by R. Courant in his solution of a torsion problem "Variational methods for the solution of problem of equilibrium and vibrations". The term "finite element method" was not due to Courant, in fact, but appears only in the 1960s on the advent of digital computers (John von Neumann, Los Alamos, 1946). In 1956 Turner, Clough, Martin and Topp with their paper "Stiffness and deflection analysis of complex structures" successfully addressed the problem of directly deriving the stiffness of a triangular panel and with this they have established the modern finite element method. By the early 1970's, finite element analysis (FEA) was limited to expensive mainframe computers owned mainly by the aeronautics, automotive, defense, and nuclear industries. From the late 1980's, the rapid drop in the cost of computers and the great increase in computing power, FEA has become a remarkably indispensable engineering and scientific tool with several available commercial modeling software.

In this thesis, a commercial software package ANSYS® - developed by John Swanson, at Swanson Analysis Systems Inc., later ANSYS Inc. – has been used. The original code was designed to model and predict transient stresses and displacements of a reactor system due to thermal and pressure loads. However, after a few years of continuous software development, several new modules were built in to the code to enable general-purpose simulations with the possibility to:

- Combine the effects of two or more different yet interrelated classes of physics (thermal, electrostatic, electrical, structural, fluid, magnetic and electromagnetic), within one unified simulation environment.
- Materials properties that are not restricted to isotropy and may change from one element to another or even within an element.
- Combine components that have different materials properties.

Nowadays, engineers and scientists extensively use commercial finite element software packages because of the easy to use/understand input and output provided via graphical user interfaces and also because of the flexibility in terms of applicable sets of element classes. This technique is highly reliable, and therefore the emphasis of the process is not laid on the mathematical know-how but on discretization and verification.

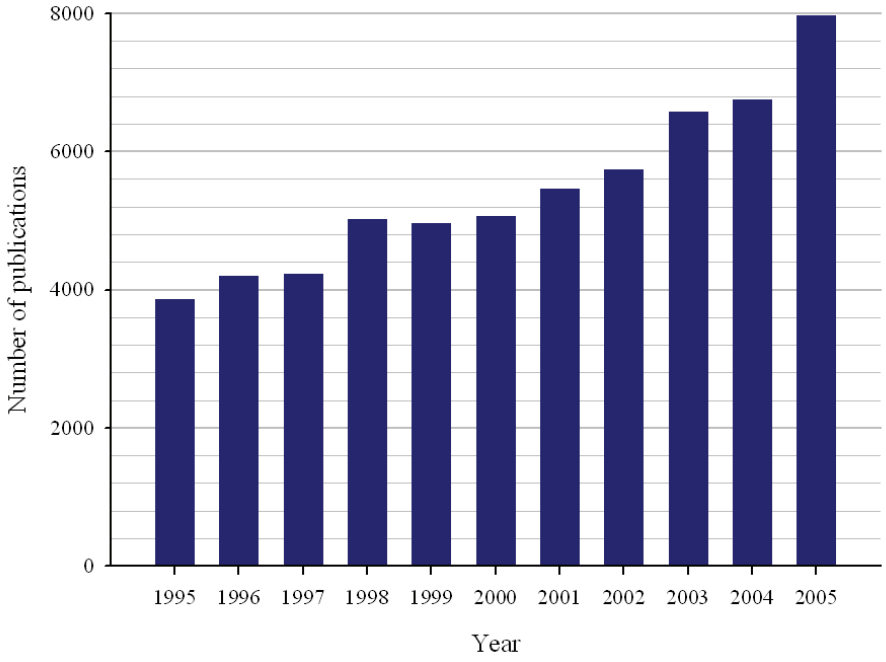

Fig. 2. Number of publications in refereed journals related to finite element method/analysis. (The data are based on the search for the relevant keywords for a particular year using the Thomson ISI search engine.)

The prevalence of published papers related to FEM is continuously increasing and doubled within the last 10 years (Fig. 2), showing that the topic is of scientific interest.

1.2 Objective and outline of the thesis

The main objective of this thesis is to show some unique cases for computer-assisted FEM solutions of thermal, mechanical and thermo-mechanical problems

related to silicon and carbon. The reasons for using the finite element method are plausible, considering that the analytical solutions for our systems were not practical, and for most of the cases, a particular phenomenon could not be revealed based on experimental investigations.

Since commercial FEM software is primarily used by industries such as automotive, aeronautical, astronautical, information technology, a further objective was to prove that scientific problems can be successfully addressed as well.

The summarized content of this thesis is as follows:

The first part of Chapter 2 shows a simple introductory modeling and experimental verification of the calculations to determine and demonstrate the capabilities of the software by modeling a heat-transfer problem in anisotropic microsystems. In a subsequent step, a similar model is applied to reveal surface temperature profiles of silicon surfaces heated with a focused laser beam. The results are used to calculate the spatial and temporal evolution of Dember and Seebeck effects in a B-doped Si wafer, and in turn to explain how micro-patterns of metallic gold could be deposited from a solution precursor on the wafers by the laser beam. Finally, an application of FEM thermal analysis is described. A novel process for laser soldering of flip-chips on transparent printed circuit boards is presented. The heat-flow problem for multi-element systems was solved to reveal the steady-state temperature maps of flip-chip and substrate assemblies in the course of a laser-soldering process. The results show that the process cannot cause any damage to the flip-chips. This is also confirmed by functionality and reliability analyses of the components.

Chapter 3 introduces a three-dimensional thermomechanical modeling on the structural changes of porous silicon samples, exposed to thermal oxidation processes at various temperatures. The method was used to support the explanations of the shifts of Si(400) peaks observed in the X-ray diffraction patterns. The strain calculated by our developed model - incorporating both intrinsic and thermal stress components – gave good quantitative match with those obtained experimentally.

In Chapter 4 – an extensive fluid-dynamic and heat-flow analysis is shown to demonstrate the validity of our measurements on chip cooling for a system in which micro-fined cooler structure made of aligned multi-walled carbon nanotube array was integrated on a heated flip-chip assembly.

Finally, the conclusions made in the thesis are presented and the further scientific applications of FEM are also discussed in Chapter 5.

2 Simulations based on heating by laser beam

2.1 Steady-state thermal analysis of temperature fields in materials under laser illumination

2.1.1 Procedure for performing FE analyses using commercial software

In the first step, the element types, element real constants, material properties, and the model geometry in the preprocessor (PREP7) are defined (ANSYS® documentation). Generally, building a finite element model requires more time than any other part of the analysis. The ANSYS® element library contains more than 150 different element types. The element type determines, among others:

- The degree-of-freedom (DOF) set (which in turn implies the discipline - structural, thermal, magnetic, electric, quadrilateral, brick, etc.)
- Whether the element lies in 2-D or 3-D space.

Most element types require inputs of materials properties. Both linear and non-linear parameters are allowed along with isotropic and orthotropic properties. The non-linear parameters are imported as tabular data. Once the materials properties are defined, the next step is to generate a finite element model - nodes and elements - that adequately describes the model geometry.
There are two methods to create a finite element model: solid modeling and direct generation. With solid modeling, the geometric shape is described, and then the geometry is automatically meshed with nodes and elements. The size and shape of the elements can be pre-set by the user. With direct generation, the location of each node together with the connectivity of each element are defined "manually".

In the second step, the SOLUTION processor is activated. Here the analysis type with appropriate options is defined, then loads or subsequent load steps are specified and applied, and finally the finite element solution is initiated. (It is also possible to apply loads using the PREP7 pre-processor.) The word load as used in this manner includes boundary conditions such as constraints, supports, or boundary field specifications, and other externally and/or internally applied stimuli, which causes the system to undergo any change. Loads in the program are divided into six categories:

1. DOF constraints
2. Forces
3. Surface loads
4. Body loads
5. Inertia loads
6. Coupled-field loads

In the third step, the SOLUTION processor initiates the calculations. Several methods of solving the system of equations are available in the ANSYS® program: sparse direct solution, preconditioned conjugate gradient (PCG) solution, Jacobi conjugate gradient (JCG) solution, incomplete Cholesky conjugate gradient (ICCG) solution, frontal direct solution, and an automatic iterative solver option (ITER). Some of these use a direct elimination of equations, while the iterative solvers obtain the solution through an iterative process, which successively refines an initial value to a solution being inside the defined tolerance of the exact solution. The software is able to choose the proper solver for a given problem; therefore the software does not require extensive knowledge from the user on the mathematical formulations.

Finally, after the solution is calculated, the postprocessors are used to review the results. Two postprocessors are available: POST1 and POST26. POST1 is the general postprocessor, to review results at one time step over the entire model or selected portion of the model. Contour displays, deformed shapes, and tabular listings can be obtained to review and interpret the results of the analysis. POST26 is the time history postprocessor, to review results at specific points in the model over any arbitrary time step. The results (data in time or frequency domain) can be plotted or exported as tabular listings.

2.1.2 Problem description

The interaction mechanisms between laser and matter depend on the parameters of the laser beam such as wavelength, spatial and temporal intensity distribution, polarization, and also on the physical and chemical properties of the materials to be processed. In general, the absorbed energy causes electronic excitations in the matter, which subsequently can induce chemical transformations and/or relaxes through vibrational processes (i.e. transforms to heat). The excitation and relaxation processes compete with each other, i.e. when the chemical conditions favor quick electron transport between the reactants, a chemical reaction occurs,

otherwise the energy is dissipated through phonons and heating of the illuminated zone takes place (Bäuerle 1996, Nánai *et al.* 2002).

To test the capabilities of ANSYS®, a simple problem was addressed concerning the steady-state spatial temperature distribution for materials heated with continuous-wave focused laser beams of Gaussian-intensity profile (Fig. 3).

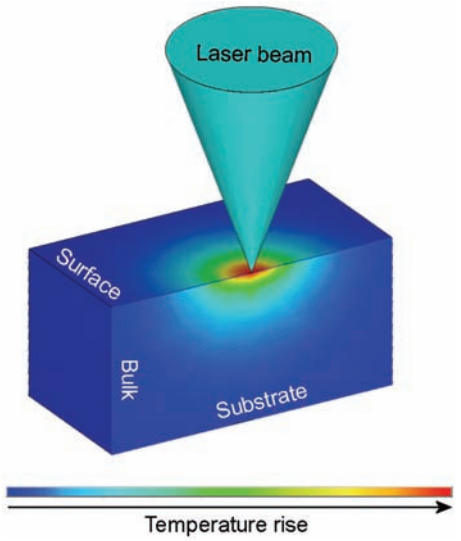

Fig. 3. Schematic drawing of the temperature rise caused by an incident laser beam.

Traditional thermal imaging techniques such as infrared thermography (Price *et al.* 2000) have insufficient spatial resolution to accurately measure the temperatures over the heat affected area, which is typically in the range of a few micrometers. In principle, micro-Raman spectroscopy (Kip and Meier 1990) and atomic force microscopy (AFM) (Rajasingam *et al.* 2003) can determine temperatures up to 1200-1300 °C with sub-micrometer spatial resolution. Nevertheless, these techniques do have their own drawbacks. Although micro-Raman spectroscopy offers a higher spatial resolution than traditional IR thermography, it lacks the sub-second recording speed. In the case of AFM-based thermal imaging, the actual temperatures cannot be determined - unless the thermal resistance between the AFM tip and the target is known (Kuball 2005). Moreover, these techniques yield no or only indirect information on the bulk temperatures. With a well-constructed finite element model, there are no such drawbacks and limitations. Therefore, a simple FE analysis was carried out to solve the steady-state, three

dimensional heat-flow in both isotropic and anisotropic materials for a heat source of a Gaussian laser spot (original publication I). To validate our model, a simple experiment was conducted. An Ar^+ laser beam (Spectra Physics 171, continuous wave, TEM_{00}, λ=488 nm, laser spot radius w_0=1.5 μm) was focused on bulk silicon, aluminum and polyimide substrates. The targeted surfaces were observed in situ with an optical microscope. The laser power was gradually increased to a point, where the surfaces just started to melt. The corresponding laser powers were detected by a power-meter integrated in the laser. These values were then used in the simulation as thermal loads.

2.1.3 Simulation

Since the materials properties are not constant in the temperature range of interest, non-linear parameters were used to enhance the accuracy of simulation results (Table 1).

Table 1. Temperature dependent materials properties (Glassbrenne and Slack 1964, Okhotin *et al.* 1972, online materials properties database: www.efunda.com, www.goodfellow.com).

Material	Density ($kg \cdot m^{-3}$)	Heat capacity ($J \cdot kg^{-1} \cdot K^{-1}$)	Thermal conductivity ($W \cdot m^{-1} \cdot K^{-1}$)
Silicon	2330	705 (300 K)	112 (300 K)
		900 (800 K)	40 (800 K)
		980 (1500 K)	23 (1500 K)
		950 (2000 K)	21 (2000 K)
Aluminum	2700	897 (300 K)	237 (300 K)
		930.6 (350 K)	240 (350 K)
		955.5 (400 K)	240 (400 K)
		994.8 (500 K)	236 (500 K)
Polyimide	1420	1090	0.36

The boundaries of the model are temperature values fixed at appropriate locations of the experimental geometry. To be able to set such fixed temperatures, the modeled volume was chosen large enough to assume a room temperature condition in the remote locations of the structure.

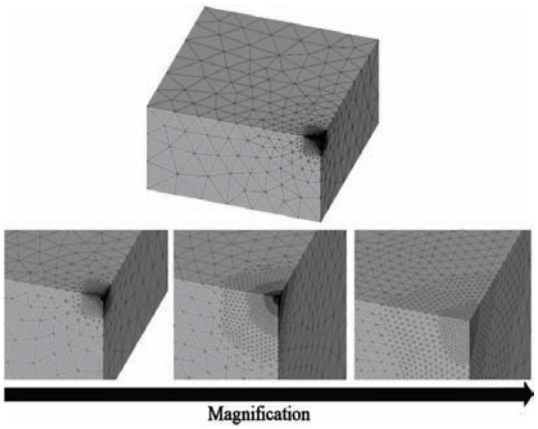

Fig. 4. The modeled volume and the increased number of elements towards the tip of the brick-like volume.

The incident beam was considered to be ideal (symmetric), therefore it is sufficient to model a quarter of the volume of interest with properly densified elements in the heat affected zone (HAZ) of the volume (Fig. 4).

The load is a heat flux function, which is the source term (Q) in the heat flow equation (Bäuerle 1996):

$$\rho\, c_p(T)\frac{\partial T(x,t)}{\partial t} - \nabla\left[\kappa(T)\nabla T(x,t)\right] + \rho\, c_p(T) v_s \nabla T(x,t) = Q(x,t)\,, \tag{1}$$

where ρ is the mass density, $c_n(T)$ is the specific heat at constant pressure, v_s is the velocity of the substrate (here equals with zero) relative to the heat source, $\kappa(T)$ is the thermal conductivity. In the source term, the Gaussian laser beam intensity distribution and also the surface reflectivity and the optical penetration are taken into account. Therefore, the source term can be written (Bäuerle 1996):

$$Q(x,t) = I(x,y,t)(1-R)\,f(z)\,, \tag{2}$$

where $I(x,y,t)$ is the time (t) dependent intensity distribution in the xy plane, R is the reflectivity of the surface and $f(z)=\alpha \exp(-\alpha z)$ describes the attenuation of the laser light in z-direction for uniform material with absorption coefficient of α. For silicon and aluminum the light intensity that penetrates into the material can be ignored (Bäuerle 1996). However for polyimide the absorption coefficient of 2.5×10^4 cm^{-1} in z direction has to be considered.

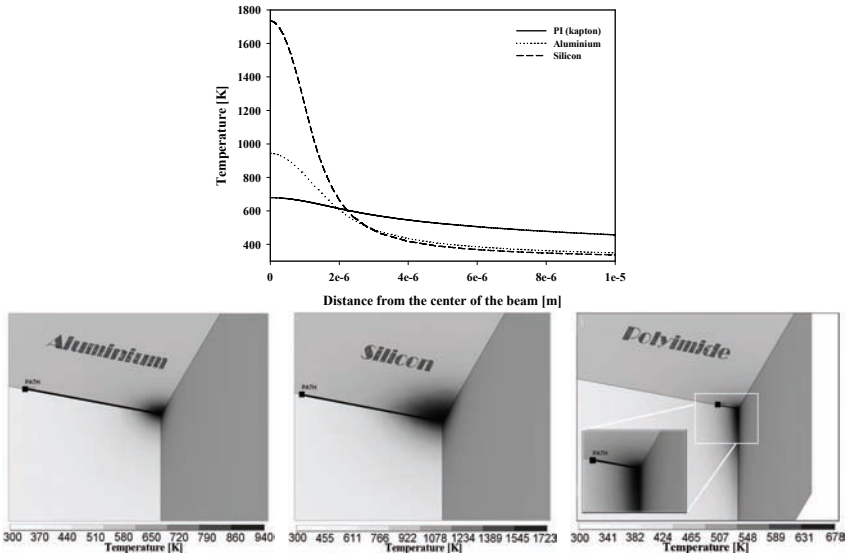

Fig. 5. (upper picture) Temperature distribution along a 10 micrometer long path and (lower pictures) the three dimensional temperature distribution in the different materials (aluminum, silicon and polyimide).

2.1.4 Conclusions

As expected, due to the low absorption coefficient the heat affected zone in polyimide is larger than in silicon or aluminum (Fig. 5). In spite of the higher melting point in silicon the heat affected zone is fairly the same as in aluminum. This effect is due to the aluminum's somewhat higher thermal conductivity. The results showed that the calculated temperatures that correspond to the laser power causing the materials to melt are very close to those of the literature data of melting temperatures for aluminum, silicon and polyimide (Table 2). Accordingly, the finite element method is fully capable to model physical problems concerning heating by a laser beam.

Table 2. Theoretical melting temperatures and modeled temperatures, which correspond to experimental laser powers that cause melting (online materials properties database: www.webelements.com, www.goodfellow.com).

Material	Melting point (K)	Laser power when melting (mW)	Modeled temp. (K)
Aluminum	934	2500	~940
Silicon	1687	640	~1720
Polyimide	525-635	15	~680

2.2 Finite element method in the course of laser-assisted deposition of metals

2.2.1 Problem description

The topic of laser-induced metal deposition from solutions and liquid precursors has turned out to be an interesting research field with the first VLSI and ULSI microelectronics devices in the mid 80s (Yokoyama *et al.* 1984, Nánai *et al.* 1989). The need for small, micrometer-size metal features on the surface of semiconductor components favored the development of novel and simple laser-assisted metallization methods for repair and prototype applications (Remes *et al.* 1997). In most cases, the formation of metal deposits is explained with photo-induced electrochemical reactions progressing at the solution-semiconductor interface due to the formed Dember potential (Schroder 2001, Mizsei 2002), U_{Dember}, and thermal electromotive force (Kireev 1978, Sze 1981), $U_{Seebeck}$. Although laser-induced metal deposition on semiconductors from aqueous precursors has been investigated widely for more than twenty years, there are several open questions still to be answered. The goal of original publication II was to reveal the spatial evolution of surface temperature and both electric potentials, which were all thought to be responsible for the localized chemical reactions in similar systems and to find plausible explanation on our experimental findings.

2.2.2 Experimental

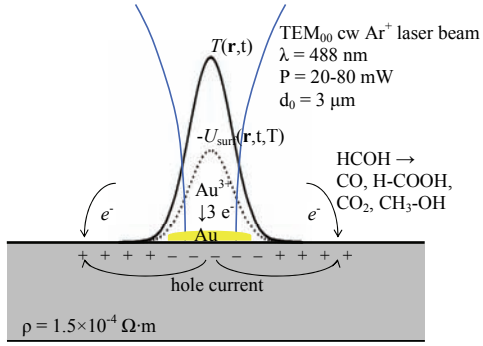

Fig. 6. Minority carriers reducing gold ions, while a hole current flows from the illuminated volume. This results in a positive surface in the dark zones, where formaldehyde is oxidized.

The experimental setup consisted of a focused Ar^+ laser (continuous wave TEM_{00} λ=488 nm, d_0=3 μm at $1e^{-1}$ intensity, P=20-80 mW, I_0=2.86×10^9–11.44×10^9 W·m^{-2}), and an *xyz* translation stage. The deposition was carried out on B-doped (ρ=1.5×10^{-4} Ω·m) Si(100) wafers immersed in aqueous electrolytes of 10^{-2} M $NaAuCl_4$ or 8×10^{-3} M $NaAuCl_4$ and 2.5 M HCOH.

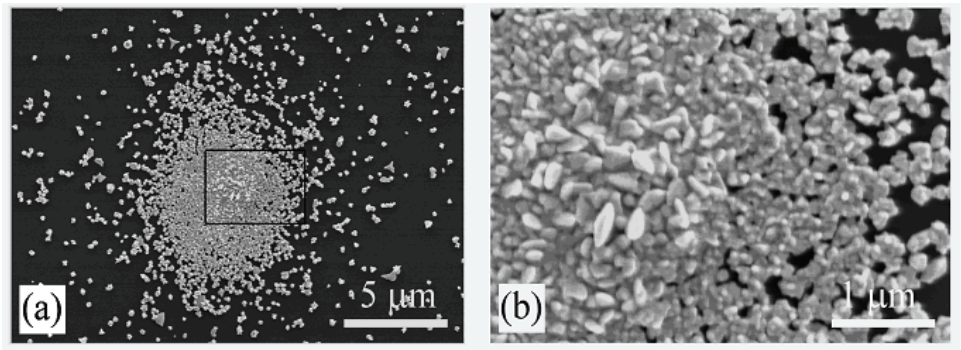

Fig. 7. (a) and (b) FESEM images of a laser-deposited gold microspot.

As observed, gold film growth could not proceed without additional formaldehyde in the precursor solution (Fig. 6). This is because the electron transfer from the surface to the Au^{3+} ions is not compensated for, and so the electric field and, consequently, the surface potential vanishes. When applying an

electron source, which is HCOH in our case, the consumed electrons are compensated for, and the localized plating process is maintained as long as the electron source is present (Fig. 7). This surface-mediated reaction mechanism is also supported with the experiments carried out on wafers with and without thermal oxide on their surface. When the surface oxide is thin and not continuous (native oxide), the charge transport is enabled via tunneling and leaking. The electron transfer through a thick thermal surface oxide layer is disabled; therefore the plating process is not possible.

2.2.3 Simulation

The time dependent three-dimensional heat-flow equation is solved numerically utilizing the finite-element method to reveal surface temperature profiles using different laser powers; and the results are used for calculating the arising Dember and Seebeck potentials. The source term (the non-reflected power density) is applied as a load (publication II):

$$c\rho\frac{\partial T}{\partial t}-\nabla(\kappa\nabla T)=\left(1-R_{air,precursor}\right)T_{precursor}\left(1-R_{precursor,Si}\right)\alpha_{opt}\,e^{-\alpha z}I_0e^{-\frac{r^2}{w_0^2}} \quad (3)$$

In the calculations, temperature dependent material parameters of silicon such as specific heat c, density ρ and thermal conductivity κ are applied. The change of surface reflectivity, due to the increasing metal coverage during the process, is ignored since the calculated values – using the Fresnel formulas – of $R_{\mathrm{precursor,Si}}$ and $R_{\mathrm{precursor,Au}}$ for smooth interfaces are very close to each other (0.28 and 0.36, respectively). In addition, the deposited gold surface has a roughness of 100-200 nm, decreasing its reflectivity so that the two values are even closer in practice. The other optical parameters are estimated to be $R_{\mathrm{air,precursor}}$=0.02, $T_{\mathrm{precursor}}$=0.98, $R_{\mathrm{precursor,Si}}$=0.28 and $\alpha_{\mathrm{opt}}=1.56\times10^{-6}\cdot\mathrm{m}^{-1}$. The results of modeling show a rapid but moderate temperature increment of the Si surface for the laser powers applied. These moderate temperatures indicate the process is governed by other than purely thermal phenomena occurring along the laser-matter interaction. According to our theory, at the beginning of the process, when there are no deposits or the gold film is transparent, the absorbed photons (hν~2.56 eV) generate electron-hole pairs, which in turn diffuse from the illuminated zone because of the formed carrier concentration gradients. Due to the higher mobility of electrons compared to the holes ($\mu_n=2.5\times10^{-2}\cdot\mathrm{m}^2\cdot\mathrm{V}^{-1}\cdot\mathrm{s}^{-1}$ and $\mu_p=1.5\times10^{-2}\ \mathrm{m}^2\cdot\mathrm{V}^{-1}\cdot\mathrm{s}^{-1}$) the illuminated

volume becomes positively charged, while negative charge accumulation takes place in the dark field, resulting in a potential difference between the bright and dark zones (Dember effect). For homogeneous illumination (i.e., charge separation in the semiconductor occurring only along the normal vector of the surface), the resulting potential is described as (Schroder 2001):

$$U_{Dember} = \frac{kT}{q}\frac{(b-1)}{(b+1)}\ln\left(1+\frac{(b+1)\Delta n}{n_0+bp_0}\right), \tag{4}$$

where $b=\mu_n/\mu_p=1.67$, and n_0 and p_0 are the equilibrium electron and hole concentrations at the temperature where the half of the acceptors are ionized. Assuming that all the photons absorbed create an electron-hole pair, the excess carrier concentration is $\Delta n(=\Delta p)=(P\alpha_{opt}\tau_{rec})\cdot(h\nu)^{-1}$, where τ_{rec} is the recombination lifetime of free carriers, which in the case of large generation rates, τ_{rec} is from 3×10^{-10} to 10^{-11} s. Thus U_{Dember} is from 1 to 3 mV for the laser power range used. It is important to point out that for intrinsic and low doping level semiconductors, the sum n_0+bp_0 in the denominator of the fraction in eq. 4 is significantly lower compared to a heavily doped semiconductor, yielding a considerable change in the surface potential. In such cases, U_{Dember} can be as high as 30 mV with a positive pole in the illuminated area and a negative ring in the dark field, resulting in an annular-shaped deposition of metal film around the laser beam.

Due to the temperature-dependent charge generation in semiconductors, an electric field $E_{Seebeck}=-\nabla U_{Seebeck}=\alpha\cdot\nabla T$ is established in the sample in which a temperature gradient ∇T exists. The phenomenon is called the Seebeck effect, and the coefficient α, which ties the potential and temperature gradients together, is the so-called thermoelectric power (or Seebeck coefficient). The thermoelectric power depends on the temperature, and on the slope of the carrier mobility versus temperature as well as on the concentration of holes. The calculated thermoelectric power is between 2.15 and 2.40 $\mathrm{mV\cdot K^{-1}}$ for the temperature range reached on the Si surface. Thus, the Seebeck potential U_{Seebeck} forms between any points of the surface having difference in their temperature. For the applied 20-80 mW laser powers, the maxima of U_{Seebeck} are between -3.6 and -17.2 mV (Fig. 8).

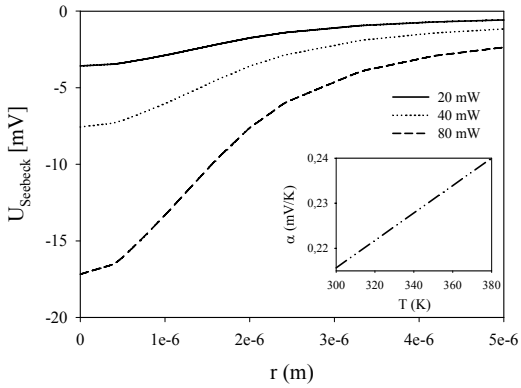

Fig. 8. Profiles of thermoelectromotive forces in equilibrium using different laser powers. The inset shows the calculated temperature dependence of the Seebeck coefficient.

Since the heated surface becomes negative, it acts as a cathode and enables the reduction of gold ions, $Au^{3+} + 3e^- \rightarrow Au$, while the dark areas undergo oxidation, $Si \rightarrow Si^{n+} + ne^-$.

It is important to point out that in equilibrium the obtained Seebeck potential is not reduced by the Dember potential, since U_{Dember} suddenly decreases and then disappears as the first gold seeds are deposited because the surface becomes shadowed from the laser beam disabling the electron-hole pair photogeneration. The temporal evolution of the two potentials can be obtained simply by combining the calculated T(t) functions with U_{Dember} and $U_{Seebeck}$.

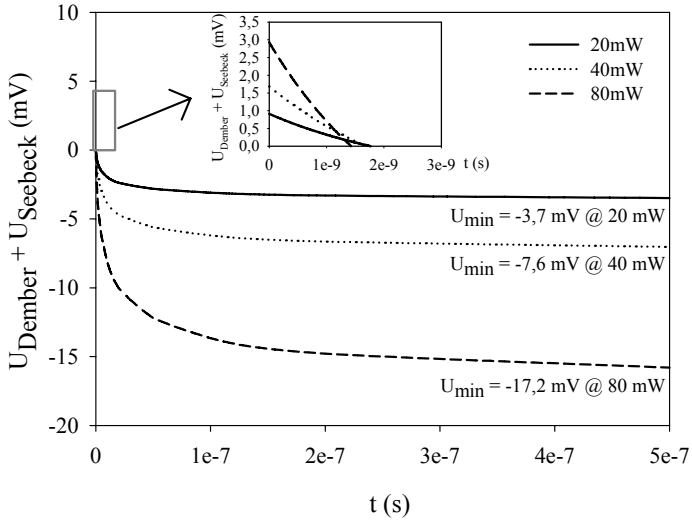

Fig. 9. Temporal evolution of the sum of UDember and USeebeck using different laser heating powers (20-80 mW). Inset shows how the positive surface potential turns to negative within 2 ns due to the Seebeck effect.

As shown in Fig. 9, the surface is positive at the beginning of the laser-silicon interaction because U_{Dember} forms right after the pair generation and diffusion. U_{Seebeck} arises together with the increasing temperature and needs ~2 ns to overcome U_{Dember}. As the surface becomes negative, the localized gold plating begins to cause a negative feedback on the Dember effect, which in turn stops, where the process is governed by the Seebeck effect.

2.2.4 Conclusions

A new approach was applied for describing both the spatial and temporal evolution of Dember and Seebeck potentials. The finite-element method was utilized to reveal surface temperature profiles under different laser powers, and the results were used for calculating the arising Dember and Seebeck potentials. The experimental observations are explained by means of a theory for charge transfer taking place between the polarized surface and the precursor. The theory supports both the dot- and ring-shaped metal deposition phenomena found

previously (Bäuerle 1996) on silicon surfaces considering the contribution of the positive Dember potential to the negative Seebeck voltage for various cases.

2.3 Novel laser-assisted soldering process supported by FEM

2.3.1 Problem description

Soldering using various lasers (CO_2, Nd:YAG, etc.) is a well-established technology applied in printed circuit board (PCB) assembly for over 20 years (Loeffler 1977, Chang 1986). In a conventional laser soldering process, the component leads - together with the solder and the PCB - are heated until the solder melts and flows around the lead and on the printed circuitry. One of the great advantages of laser soldering - compared to reflow soldering techniques – is that the applied heat is localized, thus the active regions of electronic components are not exposed to high temperatures. Therefore, assembly of heat-sensitive components can be accomplished (Semerad *et al.* 1993, Beckett *et al.* 1999, Brandner *et al.* 2000, Amako *et al.* 2001). Difficulties with the conventional laser soldering process, however, arise when area-array components are mounted, since the joints to be formed are between the component and the PCB. In such cases, the laser beam can be applied through the PCB (perpendicular to the PCB). Though the most common PCB dielectrics, FR4 and polyimide, are fairly transparent in near IR, no such applications were found in the literature.

In the original publication III, laser soldering of flip-chips on silver-on-glass substrates using a visible beam is presented. The novelty of the process is the relatively easy visualization/monitoring, by which customized circuitry fabrication and repair for high density packages becomes available. Because of the relatively large localized laser powers that are needed in the process, it was important to verify, that the soldering process is indeed a suitable alternative, when heat-sensitive components are to be assembled. Accordingly, a steady-state finite element thermal analysis was carried out to clarify the raised concerns about the possible damages caused by overheating.

2.3.2 Experimental

The electronic circuitry was made by roller-type gravure offset printing of a silver paste on ordinary soda-lime glass plates having thickness of 0.8 mm (Pudas 2004).

In the experiments, two kinds of soldering pad shapes were used. The first type of pad was thin (~2 μm) and had three parallel slits each 30 μm wide with 30 μm spacing. These samples enabled good visual monitoring of the process. The second type was thicker (~5 μm) and bulky (without any optical slits).

Flip-chips (DS18B20X digital thermometer, Dallas Semiconductor, USA) with four semi-spherical bumps (Sn5-Pb95, 350 μm in diameter) were soldered on the solder pads of circuitries applying an additional layer of Sn62-Pb36-Ag2 solder paste (Heraeus, F352). Laser soldering was carried out using a defocused (the sample is placed 500 μm behind the focal plane) beam of an Ar^+ laser. The laser spot diameters (at 1/e intensity) in the planes of focus and printed pads were ~3 μm and ~100 μm, respectively (Fig. 10).

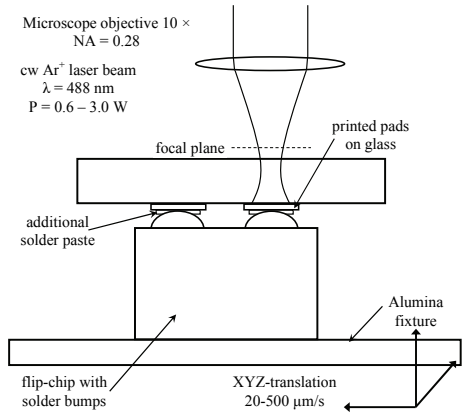

Fig. 10. Schematic experimental setup of flip-chip laser soldering.

The process was monitored using a microscope and a CCD set on the optical axis, thus direct observation during laser processing was possible. Micrographs of the solder joints were taken using optical and scanning electron microscopes (SEM, Jeol JSM-4600F). Chemical element analyses were performed on cross-sectioned samples using an EDX analyzer installed in the SEM. Thermal, electrical and mechanical tests revealed that the joints formed by our technique are of good quality (0.1 - 0.2 Ω/joint resistance and up to 7.4 MPa adhesion).

2.3.3 Simulation

In the model, approximately 130 000 elements (SOLID70 geometry), each with eight nodes (I-P) and a single degree of freedom (temperature), were used (Fig. 11).

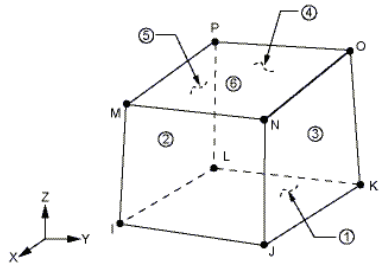

Fig. 11. The geometry, node locations and the coordinate system for SOLID70 element.

The elements, and thus the nodes, were gradually densified towards the volume of interest. Natural convection in ambient air (20 $W \cdot m^{-2} \cdot K^{-1}$ on all surface areas) was applied as boundary condition. The applied load was the heat flux generated by the Ar^{+} laser source. The effective laser intensity was evaluated by considering that the solder paste is still in solid phase below a threshold power of 2.4 W for melting. To determine the optical losses, test simulations were made by changing the relevant parameters (trial and error approach) in the heat flow equation. In addition to the given ~19% reflection loss on the optical components, a ~80% scattering/reflection loss for the silver-glass interface was obtained. Therefore the term of the heat source q in the heat-flow equation is:

$$q = (1-0.19) \times (1-0.80) \times I_0 \times \exp-(r/w)^2, \tag{5}$$

where $I_0 = P \cdot (2\pi \cdot w^2)^{-1}$, r is the distance from the center of the spot and w is the radius of the beam (~50 μm) at 500 μm distance from the focal plane.

2.3.4 Conclusions

Based on the finite element model, the heat affected zone was concluded to be well-confined into the solder pad/solder paste/chip bump region (Fig. 12).

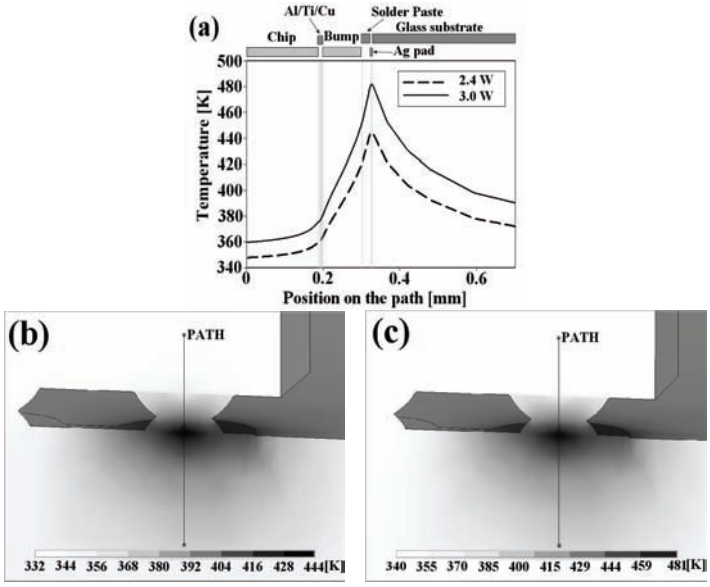

Fig. 12. Results of FEM simulation: Temperature as a function of position along the geometrical axes of a joint (a). Cross-section contour plot (temperature field) of the volume of interest for laser powers of (b) 2.4 W and (c) 3.0 W.

The peak temperature in the chip pad region is about 380 K, which implies that the heat sensitive parts of the chip (that are actually colder than the chip pad region) are prevented from damages caused by overheating. The main reason is that the SiO_x layer located between the bump and chip provides good thermal insulation; hence the chip is protected from the heat generated during the soldering process.

3 Thermomechanical modeling the structural changes of porous silicon

3.1.1 Problem description

Due to its unique materials properties porous silicon (PS) became widely studied and implemented in diverse segments of science and technology (Hérino *et al.* 1994, Kordás *et al.* 2004). A disadvantage of this material is the aging, i.e., the slow spontaneous oxidation of PS. In 1965 Beckmann observed that PS films became oxidized during long storage times in ambient air. This chemical conversion is slow and basically similar to the aging of Si wafers (Harrison and Dimitriev 1991) i.e. a native oxide layer forms on the surface of pores. Due to the ageing effect, the structural (Astrova *et al.* 2002) and optical properties (Karacali *et al.* 2003) are continuously changing. In order to avoid the transient period of aging, which is completed approximately after a year (Petrova *et al.* 2000), various oxidation processes (such as chemical, anodic, dry and wet thermal oxidation) were proposed to oxidize/passivate PS structures (Rossi *et al.* 2001, Maiello *et al.* 1997). Both partial (pre-oxidation) and full oxidation procedures are used in optical applications such as optical waveguides, photodetectors, dielectric filters and photoluminescent components.
The objective of the original publication IV was to understand and confirm the phenomena behind the residual strain formed, when oxidizing porous silicon.

3.1.2 Experimental

Porous silicon layers with 70% porosity were formed by electrochemical dark etching of boron doped (100) p^+-type silicon wafers (0.015 Ω·m). The oxidation was carried out in dry air at temperatures 473, 673, 873 and 1073 K for one hour (Pap *et al.* 2004).

During oxidation, a thermal oxide layer grows on the spongy silicon surface, where Si transforms to SiO_2 decreasing the amount (and volume) of crystalline silicon in the overall structure. Also, because the grown SiO_2 has significantly larger molar volume than that for Si, the oxide layer is forced to extend into the pores as well. The residual strain was measured by X-ray diffraction (XRD). The shift, broadening and decreased intensity of the Si (400) XRD peaks of oxidized samples showed the presence of residual stress and the decreased Si volume.

In general, for oxidized structures the obtained strain is caused by the residual stresses $\sigma_{residual}$ which is the sum of two terms (Micher *et al.* 1999, Jaccodine *et al.* 1966):

$$\sigma_{residual} = \sigma_{thermal} + \sigma_{intrinsic} \quad (6)$$

A thermal stress $\sigma_{thermal}$ forms during the cooling of the oxidized sample because of the thermal expansion coefficient (TEC) mismatch of the two materials. Besides the thermal stress, an intrinsic stress $\sigma_{intrinsic}$ is generated due to the lattice mismatch at the interface of oxide and metal/semiconductor.

3.1.3 Simulation

The finite element method is utilized to develop a computer model for simulating the porous structure and its deformation during oxidation. The porosity values used in the model are similar to those found experimentally. In order to reach such a high porosity levels (36-70%) for the structures in the model, a body centered cubic unit cell was designed and applied in the simulations (Fig. 13).

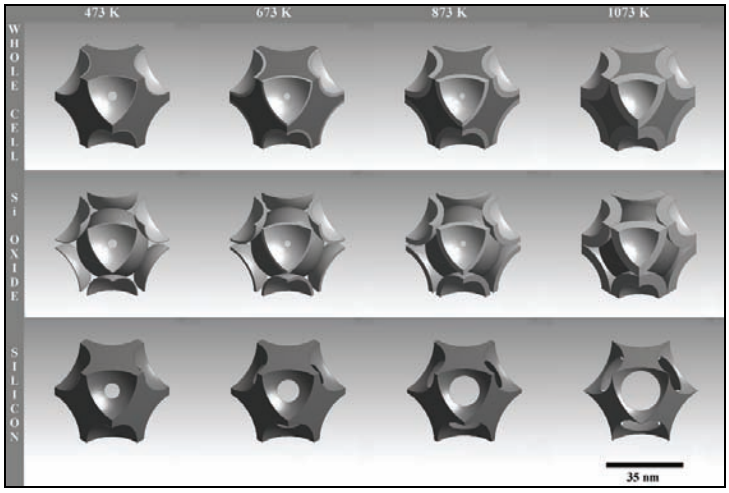

Fig. 13. Changes in the unit cell structure at different oxidation temperatures (473-1073 K). The components (silicon oxide and silicon) are separated in the second and third row for the better visibility.

The cell had a sphere-shaped pore in its centre and an eight sphere in each apex. The side of the cell was 35 nm. The pore sizes were calculated from the relative

volumes of each component in the unit cell (Pap *et al.* 2004). The diameter of pores obviously decreases with increased oxidation extent; although the diameter of the sphere representing the Si-SiO_2 interface is increasing (meaning that the Si is consumed). The sizes of the pores thus varied from 30.4 nm (as-made sample) to 24.5 nm (ox=81%), and the oxide layer thickness was between 0.5 nm (ox=9.4%) and 5.2 nm (ox=81%). The calculated parameters are shown in Table 3.

Table 3. The relative volumes and other parameters of the components during oxidation at different temperatures.

Temp / Time	ox	Si	SiO2	Porosity	Pore diameter	Oxide thickness
K / h	%	%	%	%	nm	nm
as-anodized	0	30	0	70	30.4	0
473 / 1	9.4	27	6.5	66.5	30.1	0.5
673 / 1	24	22.8	17.2	60	29.1	1.4
873 / 1	48	15.6	34.5	49.9	27.7	2.7
1073 / 1	81	5.7	58.2	36.1	24.5	5.2

Since diffraction peaks of SiO_2 were not found in the XRD pattern, the formed oxide is amorphous, and thus in the model, SiO_2 is considered to be isotropic. To enhance the accuracy of calculation, the temperature dependence of the thermal expansion coefficient (isotropic) for both materials was taken into account (Table 4).

Table 4. Materials parameters of silicon and silicon oxide used in the model (Okada and Tokumaru 1984, Ono et al 2000, online materials properties database: www.memsnet.org).

Material	Density ($kg \cdot m^{-3}$)	Molar volume ($cm^3 \cdot mol^{-1}$)	Young's modulus (GPa)	Poisson's ratio	TEC ($10^{-6} \cdot K^{-1}$)
SiO_2 (isotropic)	2197	27.31	73	0.17	0.5 (273 K)
					1.80 (1073 K)
Silicon (orthotropic)	2330	12.06	130 [100]	0.28 [100]	2.60 (273 K)
			169 [110]	0.26 [110]	3.22 (400 K)
			188 [111]	0.23 [111]	3.80 (600 K)
					4.17 (800 K)
					4.40 (1073 K)

In the analyses, symmetric boundary conditions were applied on a properly meshed unit cell (Fig. 14); hereby the out-of-plane translations and in-plane rotations, as constrains, were set to zero (for each side). Practically, it means that the unit cell is the theoretical central point of the model, and so the sides of the

cell are representing the bounds of the half space, where the symmetry occurs. The number of nodes applied was ~3×10^4 meaning an average node distance of ~0.5 nm and ~1 nm close to and far from the interfaces, respectively.

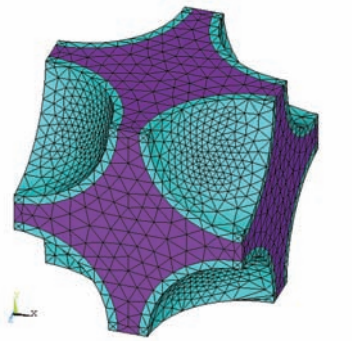

Fig. 14. An example of a meshed unit cell structure with the silicon (dark volume) and silicon oxide (light volumes).

This method allows the study of the response of the structure for different loading conditions. According to the theory, the two governing processes lead to the formation of the residual stresses during oxidation at temperatures below 1235 K. Above this temperature the stress relaxes due to the viscoelastic behavior of SiO_2 (Barla *et al.* 1986, Peng *et al.* 1991).

First, the residual strain caused by the thermal expansion coefficient (TEC) difference of Si and SiO_2 was calculated. In the model, the silicon substrate was heated up to 473, 673, 873 and 1073 K, then the elements representing the oxide layer were switched on. Finally, the temperature of the oxidized structure was decreased down to room temperature. Since the formed oxide layer has significantly lower TEC than that of the residual Si skeleton, the SiO_2 film inhibits the contraction of Si in the cooling period. As a result, e.g. after oxidation at 473 K followed by cooling to 300 K the strain in the elements is from -1.88×10^{-3} to 4.22×10^{-3} meaning that some parts of the Si skeleton are compressed while others are stretched (Fig. 15).

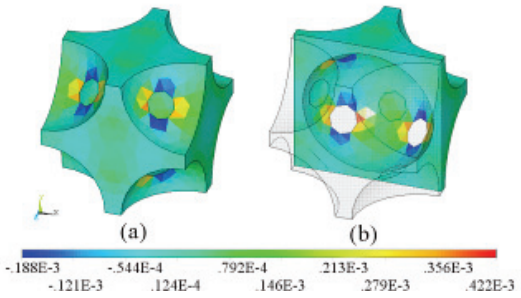

Fig. 15. (a) Residual strain due to the different TEC (along the x-axis) in the case of oxidation at 473 K and (b) the same case with cross-section plot.

In a second step, the intrinsic stress was computed for different oxide layer thicknesses and temperatures. The computed strain values were from -1.55×10^{-3} to 4.63×10^{-3} at 473 K (Fig. 16).

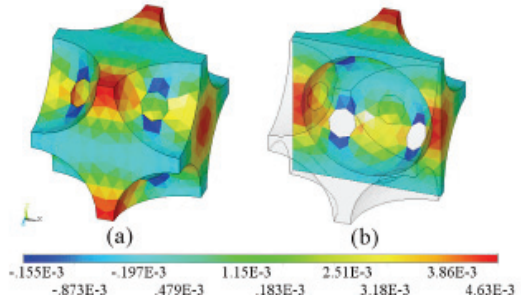

Fig. 16. (a) Intrinsic residual strain (along the x-axis) at the room temperature after oxidation at 473 K and (b) the same case with cross-section plot.

As oxidation proceeds, large stress accumulates at the Si-SiO_2 interface, because the distance between Si atoms in Si-O-Si bonds is about 30% longer than between the Si atoms in Si-Si bonds (Uematsu *et al.* 2002). The intrinsic stress values found in the literature (EerNisse 1979, Kobeda *et al.* 1988) are between 0.4 and 0.7 GPa, depending on the relative thickness of the two materials and on the geometry of the interface bonds. The as-formed stress is tensile for the Si and compressive for the amorphous SiO_2 (Buttard *et al.* 1996).

3.1.4 Conclusions

According to the nature of the XRD measurement, the obtained strain is strictly directional and gives an average value over a volume. Hence the calculated strain results, which belong to the individual elements, have to be averaged over the total volume of Si (Krawitz *et al.* 1996, Chen *et al.* 2000). In the model, this direction is the x-axis which is perpendicular to the (h00) planes.

The measured residual strain in the as-anodized PS samples was 5.5×10^{-5}, which is negligible compared to the significantly higher strain values ($>10^{-3}$) measured for the oxidized specimens.

Table 5. Modeled and measured strain in pristine and oxidized porous silicon.

Oxidation extent (oxidation temperature)	Relative volume of Si in the model	Simulated thermal residual strain	Simulated intrinsic residual strain	Simulated total residual strain	Measured strain
0 % (as-anodized)	0.3	-	-	-	5.5×10^{-5}
9.4 % (473 K)	0.2683	2.08×10^{-5}	1.67×10^{-3}	1.69×10^{-3}	2.04×10^{-3}
24 % (673 K)	0.2217	1.13×10^{-4}	1.80×10^{-3}	1.92×10^{-3}	2.48×10^{-3}
48 % (873 K)	0.1504	2.75×10^{-4}	1.98×10^{-3}	2.26×10^{-3}	5.42×10^{-3}
81 % (1073 K)	0.0639	5.06×10^{-4}	2.24×10^{-3}	2.75×10^{-3}	1.31×10^{-3} !

As it can be seen, the residual strain arises mostly from the intrinsic stress component and less from the thermal expansion difference of the two materials. The finite element method and the developed unit cell structure with the proper loading conditions made possible to understand and confirm the phenomena behind the residual strain formed, when oxidizing the porous silicon surface. The measured results of average strain (Table 5) are in good agreement with those published by Buttard *et al.* 1999, Lopez-Villegas *et al.* 1996, Manotas *et al.* 2001 and Bellet *et al.* 1996. Moreover, the calculated average strain is consistent with the experimental data i.e. the model with the two stress components describes well the experimental observations within the 473 to 873 K temperature range. The model cannot handle the drop of strain at 1073 K. The difference is because the model ignores critical materials properties such as viscoelastic behavior of SiO_2 at high temperatures, and atomic-scale local variations of stress, which might cause cracks in the residual silicon skeleton.

4 Steady state thermal-electric and CFD simulation for thermal cooling on silicon chips using carbon nanotube micro-fins arrays.

4.1.1 Problem description

The increasing integration and component density in processor components along with the associated higher power consumption necessitate an enhancement of heat dissipation from the high power devices to avoid overheating and failure (Gunther *et al.* 2001). Several solutions for component thermal management have been suggested (Strand 2004, Bar-Cohen *et al.* 1984, Simons *et al.* 1997, Tuckerman *et al.* 1981, de Boer *et al.* 2000, Peles *et al.* 2005) still there is a continuous need for developing novel cooling methods and utilizing new materials - to be able to dissipate heat in a more efficient manner. The most common method for cooling packages is the use of robust aluminum or copper pin-fin heat sinks (Lee 1995). The overall performance of a pin-fin heat sink depends on several parameters including the dimensions of the base-plate and pin-fins, thermal joint resistance, location and concentration of heat sources (Sathe *et al.* 2001). The effective cooling scheme for pin-fin heat sinks is accomplished via forced convection, where a flux of coolant (typically air) is taking up the heat from the hot fins enhancing the efficiency of the sink.

Carbon nanotubes (CNTs) are of great interest for both fundamental research and practical applications. Diamond and graphite display the highest known thermal conductivity at moderate temperatures; therefore it was likely that nanotubes and nanotube-based composites could be outstanding in this manner as well (Dresselhaus *et al.* 2000). Recent theoretical and experimental works proved that the room temperature thermal conductivity of nanotubes can be as high as 6600 $W \cdot m^{-1} \cdot K^{-1}$ (Berber *et al.* 2000), which is over 30 and 20 times larger than the thermal conductivity of aluminum and copper, respectively; which are the generally used heat sink materials in commercial appliances. However this extremely high value is only true for individual single-walled carbon nanotubes (SWCNTs). In the practical case of heat sink fabrication, where the dimensions are not on the nanoscale but in the centimeter regime, one needs to apply aligned films (or forests) of carbon nanotubes having effective thermal conductivities of ~300 and ~30 $W \cdot m^{-1} \cdot K^{-1}$ in longitudinal and transversal directions, respectively.

This value could further deteriorate due to the impurities, tube quality, and film density, which all have effect on the phonon transport i.e. on the thermal conductivity (Kilpatrick *et al.* 2006). Though such thermal conductivity is close to those for copper and aluminum, there are a number of advantages, which could lead to outperform conventional coolers. Firstly, the theoretical specific surface area for heat transfer can be as high as ~300 $m^2 \cdot g^{-1}$. Secondly, the architectures made of carbon nanotubes are light-weighted with a typical density of ~0.2 to 0.5 $g \cdot cm^{-3}$. Thirdly, there are alternatives to grow nanotube structures directly on the device, eliminating thermal interfaces between the cooler and the hot spot thus enhancing heat flow towards the cold zones. Finally, nanotubes enable geometries of coolers, which would be hardly possible to fabricate using copper or aluminum.

In the original publication V, demonstrated cooling with micro-finned nanotube coolers integrated on flip-chip assemblies are demonstrated. The applied technique employs conventional manufacturing methods thus provides an easy protocol to transfer and integrate nanotube arrays onto the presently used silicon platforms. To complement and also verify our experimental results, CFD and thermal-electric simulations on various chip/cooler assemblies were accomplished.

4.1.2 Experimental

Aligned multi-walled carbon nanotube (MWCNT) films with a thickness of ~1.2 mm were grown on Si / SiO_2 (thermal oxide, thickness of ~700 nm) by catalytic chemical vapor deposition (CCVD) at 770 °C in a tube furnace (Thermolyne 79400). The solution of 10 g ferrocene in 1000 cm^3 xylene was fed with a rate of 0.1 $cm^3 \cdot min^{-1}$ into an evaporator column pre-heated to 185 °C, from which the vapor of ferrocene and xylene was fed into the reactor by a carrier argon flow (30 $cm^3 \cdot min^{-1}$, 1 atmosphere). Deposition times of 90-120 minutes were applied.

After the synthesis, the nanotube films were chemically detached from the wafer by dissolving the SiO_2 surface layer in 7:3 vol.% mixture of ethanol and concentrated hydrofluoric acid solution. The catalyst particles (Fe) and the thin amorphous carbon layer (few microns) co-deposited at the bottom of the nanotube mats was removed by laser ablation using a defocused (~800 μm offset) 3ω Nd:YVO_4 pulsed laser having a pulse duration of τ~20 ns, repetition rate of f=100 kHz, scan rate of v=240 $mm \cdot s^{-1}$, average power of P=200 mW and spot diameter in the focal plane of d_0~15 μm. As a result, a cleaned nanotube bottom end is obtained. The same laser has been employed to etch V-shaped grooves in

the nanotube film samples to form arrays of aligned CNT fins. Typically, 15 scans at P=300 mW, f=90 kHz, v=50 mm·s^{-1} were used while maintaining the ~800 μm focal plane offset.

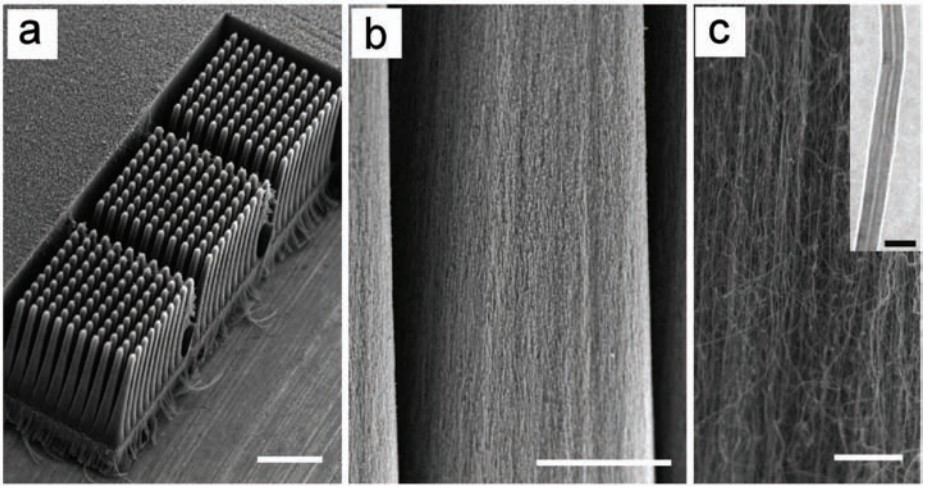

Fig. 17. Morphology and structure of laser-patterned CNT films. (a) Micro-structure of three cooler blocks laser-etched next to each other in the CNT film (scale bar 500 μm). (b) Grooves and a pyramidal fin obelisk of aligned nanotubes (scale bar 50 μm). (c) Close-up image of the aligned nanotubes (scale bar 5 μm). The inset in the figure shows an energy filtered electron microscopy (EFTEM) image of a well-graphitized nanotube (scale bar 50 nm).

The obtained nanotube pillars are held together by a non-processed thin contiguous slightly tangled layer of nanotubes at the bottom (serving as a base of the heat sink, Fig. 17a). To make the cleaned bottom surface solderable, thin chromium (50 nm) and subsequently a copper (2 μm) layer was deposited by sputtering.

For the copper fin array fabrication the same laser with different settings was used as for the CNT fin array fabrication (repetition rate of f=40 kHz, scan rate of v=500 mm/s, average power of P=1.9 W and ~360 scans). The laser focal plane was kept constant in the position of the upper facet of the Cu plate. After the laser etching, the metal blocks were treated in 3:1 vol. HCl in H_2O solution to remove surface oxides.

Si substrates including landing pads, a heating circuit and their terminations with probe pads were fabricated on Si / SiO_2 (700 nm) / Cr (50 nm) / Cu (2 μm) wafers by photo-patterning a spin-coated positive-tone resist followed by

selective wet etching of the sputtered Cu and Cr layers in 20 w/w% $Na_2S_2O_8$ and 3:1 vol. HCl in H_2O solutions, respectively. The backside of analogue temperature sensor flip-chips (LM20SITL micro-SMD, by National Semiconductor) was mechanically polished to remove the original thermal insulation layer, and then sputtered up with Cr (50 nm) and Cu (2 μm). The solder bumps (63Sn-37Pb, eutectic, T_m = 183 ºC) of the polished and metallized flip-chips were dipped in a solder flux, and then the chips were aligned and soldered at 230 ºC to the Cu landing pads (Fig. 18).

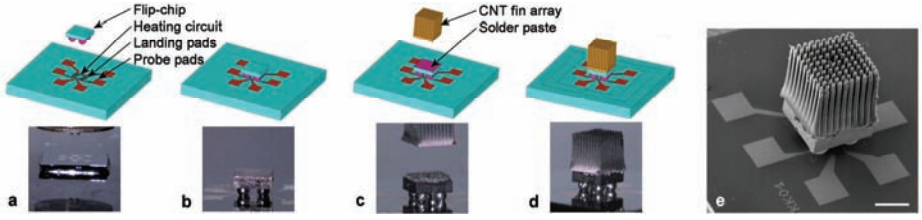

Fig. 18. Phases of substrate flip-chip/CNT-cooler assembling. (a) Positioning and (b) soldering the flip-chip on the Cu landing pads of the. (c) Solder paste dispensing, CNT array positioning and (d) soldering on the Cu coated back-side of the chip. (e) FESEM image of an assembled structure (scale bar 500 μm).[1]

In the next step, each sample has been tested on a probe-station to measure the heating power vs. chip temperature characteristics under various thermal loads (up to ~7 W) and cooling gas flow rates (N_2 at 0-2 $l \cdot min^{-1}$ through a cylindrical nozzle of 0.44 mm inner diameter).

After testing, a thin ~10 μm layer of low melting point (T_m = 96 ºC) eutectic 46Bi-34Sn-20Pb solder paste was distributed on the back of the chip, and using a fine-placer a block of nanotube cooler along its Cr/Cu sputtered side was positioned and soldered on the chip at 170 ºC. In the course of the soldering process, the finned array was pushed against the chip to squeeze out the excess solder melt to ensure the thinnest solder layer possible for the small thermal resistance.

Then the assembly was tested on the same probe-station to measure the chip temperature vs. heating power characteristics under the same range of thermal loads and cooling gas flow rates (N_2 at 0-2 $l \cdot min^{-1}$). The temperature of the heated chips is extracted from the output analogue (voltage) data of the thermometer

[1] Reprinted with permission from [Kordás K, Tóth G, Moilanen P, Kumpumäki M, Vähäkangas J, Uusimäki A, Vajtai R and Ajayan PM, Applied Physics Letters, Vol. 90, Issue 12, Page 123105 1-3., 2007]. Copyright [2007], American Institute of Physics.

chips we used in the assemblies. The Joule heat generated on the substrate by an integrated heating circuit was successfully dissipated by the nanotube-on-chip assembly resulting in a decreased chip temperature as compared to the corresponding chip without the cooling block.

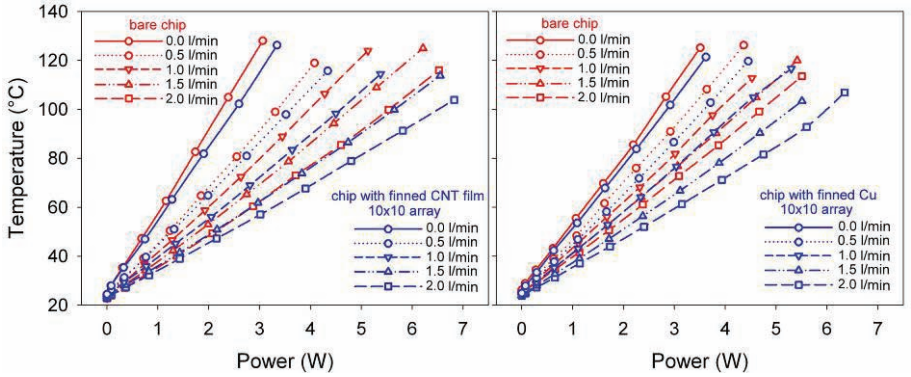

Fig. 19. Experimental results on the cooling effect of (left figure) CNT and (right figure) copper fin-arrays.[2]

Using natural convection (0.0 $l \cdot min^{-1}$), ~11% more power is observed to be dissipated from the chip that has the attached nanotube fin structures; i.e. 31.9 $mW \cdot K^{-1}$ power was dissipated instead of 28.8 $mW \cdot K^{-1}$. Under forced N_2 flow the cooling performance with the fins is improved by ~19%; i.e. 82.8 $mW \cdot K^{-1}$ of power could be dissipated instead of 69.8 $mW \cdot K^{-1}$. As for the comparison with the copper cooler, the measured temperature vs. power curves show very similar results for the two materials (Fig. 19), i.e. copper and nanotubes perform fairly equally.

These results indicate that applying the nanotube fin structure would allow the dissipation of ~30 $W \cdot cm^{-2}$ and ~100 $W \cdot cm^{-2}$ more power at 100 °C from a hot chip for the cases of natural and forced convection, respectively. As the carbon nanotube arrays form low density structures the extra power dissipated per weight of the added structure can be estimated as high as 1.1 $kW \cdot g^{-1}$ or 3.7 $kW \cdot g^{-1}$ for these two cases studied using a measured density of the nanotube films, ~0.35 $g \cdot cm^{-3}$.

[2] Reprinted with permission from [Kordás K, Tóth G, Moilanen P, Kumpumäki M, Vähäkangas J, Uusimäki A, Vajtai R and Ajayan PM, Applied Physics Letters, Vol. 90, Issue 12, Page 123105 1-3., 2007]. Copyright [2007], American Institute of Physics.

4.1.3 Simulation

Computational fluid dynamics and thermal-electric finite element models were developed to study the steady-state laminar coolant flow and temperature distribution for both finned and also for bare reference chips.

CFD model

The ANSYS®/FLOTRAN CFD offers comprehensive tools for analyzing two-dimensional and three-dimensional fluid flow fields. Since the study of turbulent and transitional flow conditions are beyond of the scope of this thesis, the model is limited to the laminar flow regime with Reynolds number of ~1800 at the nozzle exit for 0.5 $l \cdot min^{-1}$ flow rate. In the case of laminar flow, the velocity field is assumed to be well-ordered and smooth, as it is in highly viscous, slow-moving flows.

The ANSYS® FLOTRAN has two types of elements, FLUID141 and FLUID142, for two- and three-dimensional flow cases. For these elements, the ANSYS® program calculates velocity components, pressure, and temperature from the conservation of mass, momentum and energy. In the simulation, a simplified geometry with 670 000 elements were used. The inlet was the nozzle with the applied flow speed of 55 $m \cdot s^{-1}$ (corresponding to the 0.5 $l \cdot min^{-1}$ N_2 flow rate) the outlets (where the pressure was set to zero) were the sides and the top surface of the modeled volume. On the remaining facets (as they were assumed to be a wall) the speed values were set to zero.

Steady state solutions (using 100 iterations) were computed. The results showed significantly different flow fields for bare and finned chips (Fig. 20).

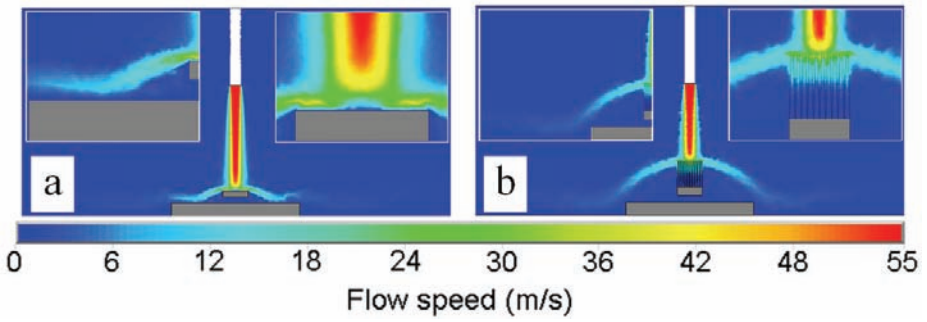

Fig. 20. Color plot of the flow field in case of (a) the bare chip and (b) the added cooler with 10x10 fins. [3]

According to the obtained velocities, in case of bare chip, the silicon substrate plays significant role in the cooling since the nitrogen gas flows over the surface with a significant speed of ~20 $m \cdot s^{-1}$. On the other hand, the finned CNT heat sink was partially penetrated by the impingement flow but in the same time the fin prohibits the flow over the silicon substrate by deflecting it. These results gave good account for the proper loading conditions for the second part where the object was to determine the steady state temperature distribution by thermal-electric simulation.

Thermal-electric model

At this stage of the simulation, the CAD (computer assisted design) geometry of landing pads, a heating circuit, their terminations and the probe pads were imported into the ANSYS® together with the official layout of the temperature sensor flip-chip (Fig. 21).

[3] Reprinted with permission from [Kordás K, Tóth G, Moilanen P, Kumpumäki M, Vähäkangas J, Uusimäki A, Vajtai R and Ajayan PM, Applied Physics Letters, Vol. 90, Issue 12, Page 123105 1-3., 2007]. Copyright [2007], American Institute of Physics.

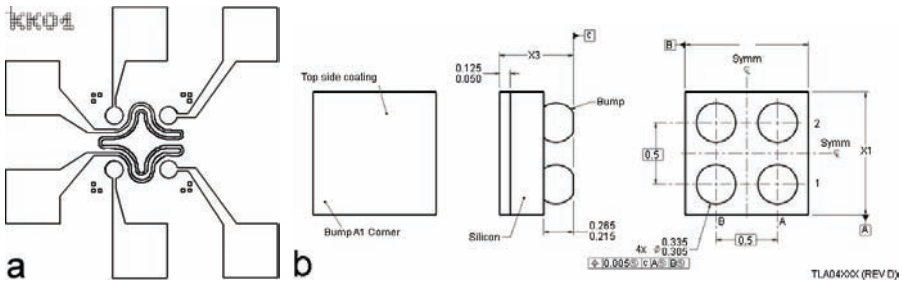

Fig. 21. (a) CAD design for the heating circuit/landing pads and (b) the factory layout of the sensor chip.

In the model, approximately 90 000 previously discussed SOLID70 and 15 000 SOLID69 type elements (for the copper heating circuit) were used. This latter element type has a three-dimensional thermal and electrical conduction capability (two degrees of freedom: temperature and voltage). Joule heat generated by the current flow is also included in the heat balance. The element is defined by eight nodes and the material properties (density, heat capacity, thermal conductivity). The electrical material property is the resistivity of the material. The resistivity, like the other material properties, was taken into account as a function of temperature (Table 6).

Table 6. Temperature dependent materials properties (Glassbrenne and Slack 1964, Okhotin *et al.* 1972, Lide 1991, online materials properties database: www.efunda.com, www.indium.com, www.accuratus.com).

Material	Density ($kg \cdot m^{-3}$)	Heat capacity ($J \cdot kg^{-1} \cdot K^{-1}$)	Thermal conductivity ($W \cdot m^{-1} \cdot K^{-1}$)	Electrical resistivity $\Omega \cdot m \times 10^{-8}$
Silicon	2390	705 (298 K)	191 (250 K)	N/A
		757 (350 K)	148 (300 K)	
		788 (400 K)	119 (350 K)	
		830 (500 K)	98 (400 K)	
		859 (600 K)	76 (500 K)	
			61 (600 K)	
Copper	8960	385 (298 K)	406 (250 K)	3.916 (295 K)*
		393 (350 K)	401 (300 K)	
		399 (400 K)	396 (350 K)	5.632 (500 K)*
		408 (500 K)	393 (400 K)	
		417 (600 K)	386 (500 K)	7.366 (700 K)*
			379 (600 K)	
63Sn-37Pb	8410	200	25	N/A
46Bi-34Sn-20Pb	8410	200	25	N/A
Alumina	3700	900	35	N/A
MWCNTs	100	300 (200 K)	300	N/A
		400 (250 K)	(axial)	
		500 (300 K)	30 (perpendicular)	

*values found in the literature are multiplied by factor of 2.2 due to the difference between the bulk and deposited copper composition, and the somewhat different geometry.

Two thermal loads were applied: (i) Voltage on the closing facets of the heating circuit terminations to cause current and consequently the Joule heat (Fig. 22) and (ii) local heat transfer coefficients (as convection) h empirically obtained from the velocity values of the corresponding flow fields.

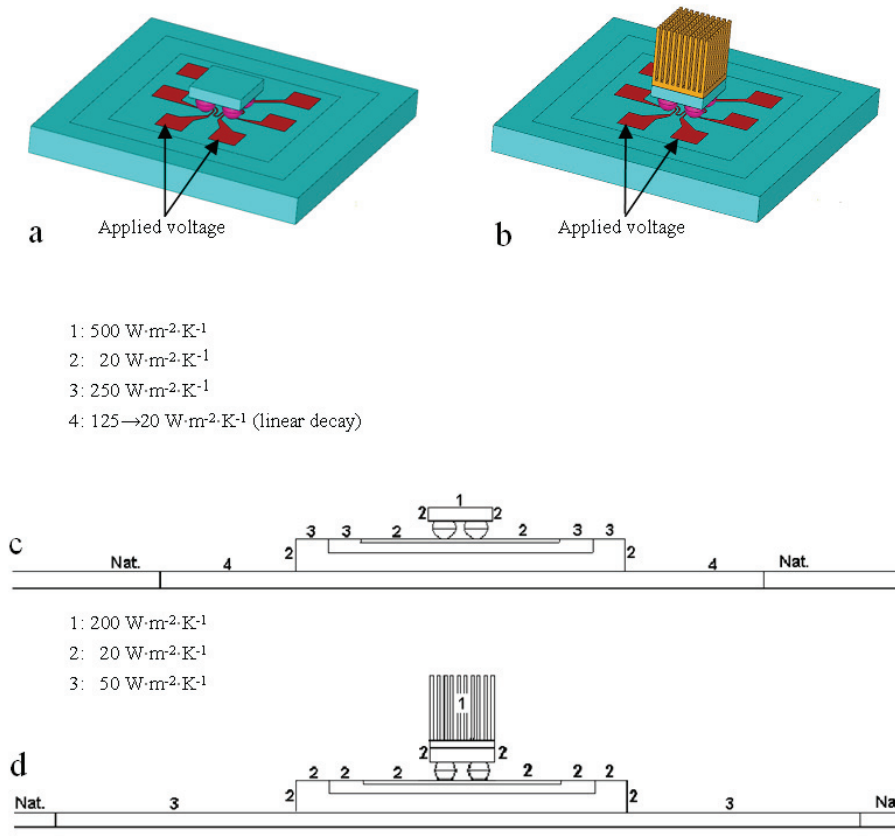

Fig. 22. Part of the modeled volume including the silicon substrate and (a) the bare chip and (b) chip with the added fin-array. (c)-(d) The local heat transfer coefficients applied at various locations of the assemblies.

As boundary conditions, the sides were assumed to be at room temperature. Because of the relatively low temperatures and small surface areas of the hot spots, the losses caused by heat radiation were neglected in the thermal model, i.e. the heat transport is restricted to conductive and convective fluxes. The solution output (in this case a color plot of temperature) is shown in Fig. 23.

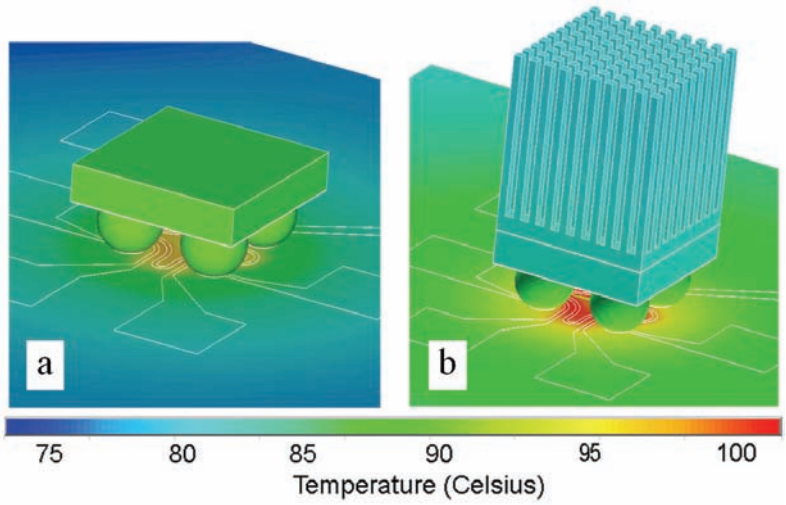

Fig. 23. Temperature field plotted for (a) bare chip and (b) cooled chip.[4]

4.1.4 Conclusions

The FEM turned out to be a great tool for investigating the flow and temperature fields throughout the project. The simulated values are reliable and in a good agreement with the measured temperatures (Fig. 24).

[4] Reprinted with permission from [Kordás K, Tóth G, Moilanen P, Kumpumäki M, Vähäkangas J, Uusimäki A, Vajtai R and Ajayan PM, Applied Physics Letters, Vol. 90, Issue 12, Page 123105 1-3., 2007]. Copyright [2007], American Institute of Physics.

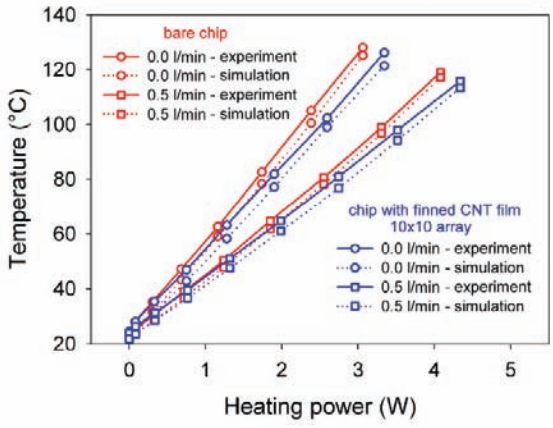

Fig. 24. Comparison between the measured and modeled temperature values for both bare and CNT equipped chips.[5]

With the aid of computer assisted finite element method, a novel and efficient cooling technique is demonstrated for chip thermal management using laser-patterned MWCNT fins transferred and mounted on the backside of a chip. The achieved cooling efficiency is in the range of future microprocessor needs (~100 $W \cdot cm^{-2}$), therefore the carbon nanotube coolers could serve as excellent hot-spot removers with their high thermal conductivity. The application of the finite element software was a significant part of the work as it provided essential information on the flow and subsequently also on the obtained temperature fields showing the differences between the different chip assemblies. With the aid of FEM, even more efficient and larger CNT coolers can be designed and modeled, since there are several key areas such as fin-array geometry/location, nanotube forest density and better gas flow efficiency along with the superior and optimized chip-nanotube thermal interface.

[5] Reprinted with permission from [Kordás K, Tóth G, Moilanen P, Kumpumäki M, Vähäkangas J, Uusimäki A, Vajtai R and Ajayan PM, Applied Physics Letters, Vol. 90, Issue 12, Page 123105 1-3., 2007]. Copyright [2007], American Institute of Physics.

5 Summary and conclusions

In the present thesis, some unique cases for computer-assisted FEM solutions of thermal, mechanical and thermo-mechanical problems related to electrical materials/components made of silicon and carbon were presented.

Test simulations were carried out for a heat-transfer problem in both isotropic and anisotropic materials. The capabilities of a commercial software package were demonstrated by solving a steady-state spatial temperature distribution on the surface and in the bulk of aluminum, silicon and polyimide under an illumination with a continuous-wave focused laser beam of Gaussian-intensity profile. The calculations were verified with experiments, in which melting of the above materials were induced by the laser beam. The laser powers used in the experiments were applied as a source power in the modeling. The calculated peak temperatures had good match with the corresponding melting temperatures of the materials we investigated.

In the following task, a similar model was utilized to reveal surface temperature profiles of silicon surfaces heated with a focused laser beam. The results - i.e. the spatial and temporal evolution of temperature - were used to evaluate the role of Dember and Seebeck effects in a laser-assisted metal deposition process of gold from aqueous precursors on boron-doped p^+-Si wafers. As revealed the negative surface potential arising in the heated regions due to the Seebeck effect can compensate for the positive potential of the photoelectric Dember effect, and in turn gold ions are reduced to metallic gold to yield microscopic patterns of gold deposits on the surface.

Next, a novel process for laser soldering of flip-chips on silver solder pads that were printed on transparent glass substrates was demonstrated. There, the heat-flow problem for a multi-element system was solved to reveal the steady-state temperature maps of the flip-chip and substrate assemblies in the course of a laser-soldering process. The results showed the process would not cause any damage to the flip-chips, as also confirmed by functionality and reliability analyses of the components.

In the following, a unique three-dimensional thermo-mechanical model on the structural changes of thermally oxidized porous silicon was developed to explain the shifts of Si(400) peaks observed by X-ray diffraction. The strain calculated by the developed model – incorporating both intrinsic and thermal stress components – gave good quantitative match with those obtained experimentally, and proved that the intrinsic stress component plays the decisive

role in the tensile stress in the residual silicon skeleton after the partial oxidation of porous silicon films.

At last, an extensive fluid-dynamic and heat-flow analysis was developed to support our measurements on chip cooling with micro-fined cooler structures made of highly-aligned multi-walled carbon nanotube films that were integrated on a heated flip-chip assembly. The flow simulations - i.e. velocity field of the coolant nitrogen gas flow - helped us to construct good loading conditions with reasonable film coefficients for the thermal-electric modeling, and in turn enabled us to explain the peculiarities of the experimentally observed cooling.

In this thesis, the feasibility and limitations of FEM simulations using commercial software were studied. The computer-assisted finite element modeling proved to be an efficient, versatile and relatively easy-to-use tool to solve scientific problems, where analytical solutions were not practical or not possible at all; and for most of the cases, direct explanation of a particular phenomenon by experiments only could not be made.

The studied cases also pointed out the weaknesses and the reasonable application areas of the computer assisted finite element method. First of all, the work is to start with an extensive study and search on materials properties and with the construction of the appropriate geometry of the system. Collecting temperature (and in some cases pressure) dependent materials properties is not a straightforward task. The author of this thesis was many times surprised how inconsistent data are available in the literature. Determining the precise dimensions of the modeled structure has a great importance as well. As experienced, for most commercial components the geometry and materials composition are not available (because of the industrial confidentiality and patenting issues) or not accurate enough. Therefore, it is suggested to carry out imaging/measurement with various microscopy techniques such as SEM, TEM and AFM to reveal the real dimensions, and also to study the elemental and chemical composition of the materials using EDX or other spectroscopy techniques. Amongst others, the properly set density of the computational elements is also very important. Too large or highly distorted elements could lead to inaccurate analysis due to averaging of the solution output (both temporal and spatial resolution loss) meanwhile too high density of nodes requires enormous computing power. As a trade-off, the best alternative to overcome such difficulties is the utilization of high density nodes only at the locations, where large gradients of the calculated physical quantities are expected. Also, if the system bears with

any symmetry, it is useful to take an advantage of that to reduce the element number.

In straightforward cases, where the loading conditions are not too complex, the structure is fairly simple and the temperature/pressure dependent materials properties are known, predictions and system analysis can be based entirely on simulations. The author of this thesis is confident the results obtained from the simulations are correct and accurate. Nevertheless, achieving a reliable model was increasingly difficult as the structure in question became more and more complex. In the course of thermal-electric and flow modeling the author realized, not all the systems could be simplified to a level where they could be trustworthily modeled. It is relatively easy to introduce an error, e.g. by employing a slightly different geometry in the model than that of the real system. We cannot disregard the fact that in any fabrication process, deposited film thickness and also the applied chemical etching to fabricate any pattern never results in exactly the same homogenous and rectangular structure what we intend to use in the model. Therefore, it is always recommended to compare the computed findings with the experimental results in as many steps of the work as possible.

References

Accuratus Corporation [online], [Cited May 3, 2007] Available from: http://www.accuratus.com.

Amako J, Umetsu K & Nakao H (2001) Laser soldering with light-intensity patterns reconstructed from computer-generated holograms. Appl Opt 40(31): 5643-5649.

ANSYS® documentation [online], [Cited May 3, 2007], Available from: http://www.ansys.com.

Astrova EV, Ratnikov VV, Remenyuk AD & Shul'pina IL (2002) Strains and crystal lattice defects arising in macroporous silicon under oxidation. Semiconductors 36(9): 1033-1042.

Bar-Cohen A & Rohsenow WM (1984) Thermally optimum spacing of vertical, natural convection cooled, parallel plates. J Heat Transf ASME 106: 116-123.

Barla K, Herino R & Bomchil G (1986) Stress in oxidized porous silicon layer. J Appl Phys 59(2): 439-441.

Bäuerle D (1996) Laser Processing and Chemistry: Springer-Verlag, Berlin: 387-396.

Beckett PM, Fleming AR, Gilbert JM & Whitehead DG (1999) The laser in manufacture– its use in the soldering of electronic assemblies. Trans Inst Meas Control 21(1): 2–7.

Beckmann KH (1965) Investigation of the chemical properties of stain films on silicon by means of infrared spectroscopy. Surf Sci 3(4): 314-332.

Bellet D & Dolino G (1996) X-ray diffraction studies of porous silicon. Thin Solid Films 276(1-2): 1-6.

Berber S, Kwon Y-K & Tománek D (2000) Unusually high thermal conductivity of carbon nanotubes. Phys Rev Lett 84(20)**:** 4613-4616.

Boer MJ, Tjerkstra RW, Berenschot JW, Jansen HV, Burger GJ, Gardeniers JGH, Elwenspoek M & van den Berg A (2000) Micromachining of buried micro channels in silicon. J Microelectromech Syst 9(1): 94-103.

Brandner M, Seibold G, Chang C, Dausinger F & Hugel H (2000) Soldering with solid state and diode lasers: Energy coupling, temperature rise, process window. J Laser Appl 12(5): 194–199.

Buttard D, Bellet D & Dolino G (1996) X-ray-diffraction investigation of the anodic oxidation of porous silicon. J Appl Phys 79(10): 8060-8070.

Buttard D, Dolino G, Faivre C, Halimaoui A, Comin F, Formoso V & Ortega L (1999) Porous silicon strain during in situ ultrahigh vacuum thermal annealing. J Appl Phys 85(10): 7105-7111.

Carlos AF (2004) Introduction to finite element methods. University of Colorado, Boulder [online]. [Cited May 3, 2007], Available from: http://www.colorado.edu/engineering/CAS/courses.d/IFEM.d/Home.html.

Castigliano CAP (1966) The theory of equilibrium of elastic systems and its applications. Dover Publications, New York. Translated from Castigliano's "Théorem de l'equibre des systèmes élastiques et ses applications" by Andrews E S.

Chang DU (1986) Experimental investigation of laser beam soldering. Weld J 65(10): 33-41.

Chen CR, Qin SY, Li SX & Wen JL (2000) Finite element analysis about effects of particle morphology on mechanical response of composites. Mater Sci Eng A-Struct Mater Prop Microstruct Process 278(1-2): 96-105.

Courant R (1943) Variational methods for the solution of problems of equilibrium and vibrations. B Am Math Soc 49: 1-23.

Lide DR (ed) (1991-1992) CRC Handbook of Chemistry and Physics 72nd edition. CRC press, Boston.

Dresselhaus MS & Eklund PC (2000) Phonons in carbon nanotubes. Adv in Physics 49(6): 705-814.

EerNisse EP (1979) Stress in thermal SiO_2 during growth. Appl Phys Lett 35(9): 8-10.

Engineering fundamentals [online], [Cited May 3, 2007], Available from: http://www.efunda.com.

Galerkin BG (1915) Series solution of some problems in elastic equilibrium of rods and plates. Vestnik Inzhenerov i Tekhnikov 19: 897-908.

Gunther SH, Binns F, Carmean DM & Hall JC (2001) Managing the impact of increasing microprocessor power consumption. Intel Technology Journal 5(1) [online], [Cited May 3, 2007], Available from: http://www.intel.com/technology/itj/q12001/pdf/art_4.pdf.

Glassbrenner CJ & Slack GA (1964) Thermal Conductivity of Silicon and Germanium from 3°K to the Melting Point. Phys Rev 134(4A): 1058-1069.

Goodfellow [online], [Cited May 3, 2007], Available from: http://www.goodfellow.com.

Harrison HB & Dimitriev S (1991) Ultra-thin dielectrics for semiconductor applications–growth and characteristics. Microel J 22(2): 3-38.

Hérino R & Lang W (eds) (1995) European Materials Research Society 1994 Spring Conference, Symposium F: Porous Silicon and Related Materials, Thin Solid Films 255(1-2): 1-333.

Indium Corportion [online], [Cited May 3, 2007], Available from: http:// www.indium.com.

Jaccodine RJ & Schlegel WA (1966) Measurement of strains at Si-SiO_2 iInterface. J Appl Phys 37(6): 2429-2434.

Karacali T, Cakmak B & Efeoglu H (2003) Aging of porous silicon and the origin of blue shift. Optics Express 11(10): 1237-1242.

Kilpatrick SJ, Geil BR, Ibitayo D, Zheleva TS, Ervin MH, Wickenden AE, Ajayan PM, Talapatra S, Li X, Ci L, Kar S, Soldano C, Vispute RD, Hullavarad SS & Venkatasan T (2006) Carbon nanotube arrays as next generation heat dissipation layers for high heat flux devices. 25th Army Science Conference USA [online], [Cited May 3, 2007], Available from: http://www.asc2006.com/posters/MP-03.pdf.

Kip BJ & Meier RJ (1990) Determination of the local temperature at a sample during Raman experiments using Stokes and anti-Stokes Raman bands. Appl Spectrosc 44(4): 707-711.

Kireev PS (1978) Semiconductor Physics. Mir Publishers, Moscow: 318-334.

Kobeda E & Irene EA (1988) SiO_2 film stress-distribution during thermal-oxidation of Si. J Vac Sci Technol B6(2): 574-578.

Kordás K, Beke Sz, Pap AE, Uusimäki A & Leppävuori S (2004). Optical properties of porous silicon. Part II: Fabrication and investigation of multilayer structures. Opt Mater 25(3): 257-260.

Kordás K, Pap AE, Beke Sz & Leppävuori S (2004) Optical properties of porous silicon. Part I: Fabrication and investigation of single layers. Opt Mater 25(3): 251-255.

Krawitz AD, Winholtz RA & Weisbrook CM (1996) Relation of elastic strain distributions determined by diffraction to corresponding stress distributions. Mater Sci Eng A-Struct Mater Prop Microstruct Process 206(2): 176-182.

Kuball M (2005) Complementary techniques expose GaN transistor defects. Compound Semiconductor 10 [online], [Cited May 3, 2007], Available from: http://compoundsemiconductor.net/articles/magazine/11/10/3/1.

Lee S (1995) How to select a heat sink. Electronics Cooling 1(1): 10-14.

Loeffler JR (1977) N/C laser soldering- Fast. Low cost. No rejects. Assembly and Fastener Eng 20(3): 32-34.

Lopez-Villegas JM, Navarro M, Papadimitriou D, Bassas J & Samitier J (1996) Structure and non-uniform strain analysis on p-type porous silicon by X-ray reflectometry and X-ray diffraction. Thin Solid Films 276(1-2): 238-240.

Maiello G, Monica SL, Ferrari A, Masini G, Bondarenko VP, Dorofeev AM & Kazuchits NM (1997) Light guidind in oxidized porous silicon optical waveguides. Thin Solid Films 297(1-2): 311-313.

Maiman TH (1960) Stimulated Optical Radiation in Ruby. Nature 187(4736): 493-494.

Manotas S, Agullo-Rueda F, Moreno JD, Ben-Hander F & Martinez-Duart JM (2001) Lattice-mismatch induced-stress in porous silicon films. Thin Solid Films 401(1-2): 306-309.

Michler J, Mermoux M, Kaenel Y, Haouni A, Lucazeau G & Blank E (1999) Residual stress in diamond films: origins and modeling. Thin Solid Films 357(2): 189–201.

Mizsei J (2002) Fermi-level pinning and passivation on the oxide-covered and bare silicon surfaces and interfaces. Vacuum 67(1): 59-67.

Nánai L, Hevesi I, Bunkin FV, Luk'yanchuk BS, Brook MR, Shafeev GA, Jelski DA, Wu ZC & George TF (1989) Laser-induced metal deposition on semiconductors from liquid electrolytes. Appl Phys Lett 54(8): 736-738.

Nánai L, Kordás K, Leppävuori S & George TF (2002) Chemistry of materials metallization. In George TF (ed) Modern Topics in Chemical Physics, Research Signpost, Kerala, India

Nelson DF & Boyle WS (1962) A continuously operating ruby optical maser. Appl Optics 1: 181-183.

Okada Y & Tokumaru Y (1984) Precise determination of lattice parameter and thermal expansion coefficient of silicon between 300 and 1500 K. J Appl Phys 56(2): 314-320.

Okhotin AS, Pushkarskii AS & Gorbachev VV (1972) Thermophysical Properties of Semiconductors. "Atom" Publ. House, Moscow (in Russian).

Ono N, Kitamura K, Nakajima K & Shimanuki Y (2000) Measurement of Young's Modulus of Silicon Single Crystal at High Temperature and Its Dependency on Boron Concentration Using the Flexural Vibration Method. Jpn J Appl Phys 39: 368-371.

Pap AE, Kordás K, George TF & Leppävuori S (2004) Thermal oxidation of porous silicon: Study on reaction kinetics. J Phys Chem B 108(34): 12744-12747.

Peles Y, Kosar A, Mishra C, Kuo C-J & Schneider B (2005) Forced convective heat transfer across a pin fin micro heat sink. Int J Heat Mass Transfer 48(17): 3615-3627.

Peng, JP, Chidambarrao D & Srinivasan GR (1991) Novel. A nonlinear viscoelastic model for thermal oxidation of silicon. COMPEL - The International Journal for Computation and Mathematics in Electrical and Electronic Engineering 10(4): 341-353.

Petrova EA, Bogoslovskaya KN, Balagurov LA & Kochoradze GI (2000) Room temperature oxidation of porous silicon in air. Mat Sci Eng B-solid 69(70): 152-156.

Price DM, Reading M, Hammiche A & Pollock HM (2000) New adventures in thermal analysis. J Therm Anal Calorim 60(3): 723-733.

Rajasingam S, Sarua A, Kuball M, Cherodian A, Miles MJ, Younes CM, Yavich B, Wang WN & Grandjean N (2003) High-temperature annealing of AlGaN: Stress, structural, and compositional changes. J Appl Phys 94(10): 6366-6371.

Rayleigh JWS (1945) The theory of sound Volume I-II. 2nd edition Dover Publications, New York.

Remes J, Moilanen H & Leppävuori S (1997) Laser-assisted chemical vapor deposition of nickel and laser cutting in integrated circuit restructuring. Phys Scr T69: 268-272.

Ritz W (1908) Über eine neue methode zur lösung gewisser variationsproblem der mathematischen physic. J Reine Angew Math 135: 1-61.

Rossi AM, Amato G, Camarchia V, Boarnio L & Borini S (2001) High-quality porous-silicon buried waveguides. Appl Phys Lett 78(20): 3003-3005.

Pudas M (2004) Gravure-offset printing in the manufacture of ultra-fine-line thick-films for electronics. Acta Universitatis Ouluensis C 201 [online] Oulu University Library, Oulu, [Cited May 3, 2007], Available from: http://herkules.oulu.fi/isbn9514273036/.

Sathe SB, Calmidi VV & Stutzman RJ (2001) Parameters affecting package thermal performance - a low end system level example. Electronics Cooling 7(2): 44-51.

Schroder DK (2001) Surface voltage and surface photovoltage: history, theory and applications. Meas Sci Technol 12: R16-31.

Semerad E, Nicolics J & Musiejovszky L (1993) Laser soldering of surface-mounted devices for high-reliability applications. J Mater Sci 28(18): 5065-5069.

Simons RE, Antonetti VW, Nakayama W & Oktay S (1997) Heat transfer in electronic packages in Microelectronics Packaging Handbook, Ch. 4, Chapman & Hall, New York.

Strand SD (2004) Future power technology in the global marketplace. Applied Power Electronics Conference and Exposition APEC '04. Nineteenth Annual IEEE 1: 18-23.

Sze SM (1981) Physics of Semiconductor Devices. Wiley, New York: 28-29.

Timoshenko SP (1921) On the correction for shear of the differential equation for transverse vibration of prismatic bars. Philos Mag 41(6): 744-746.

Tuckerman DB & Pease RFW (1981) High-performance heat sinking for VLSI. IEEE Electr Device L 2(5): 126-129.

Turner MJ, Clough RW, Martin HC & Topp LJ (1956) Stiffness and deflection analysis of complex structures. J Aeronaut Sci 38: 805-823.

Uematsu M, Kageshima H & Shiraishi K (2002) Microscopic mechanism of thermal silicon oxide growth. Comput Mater Sci 24(1-2): 229-234.

Yokoyama H, Kishida S & Washio K (1984) Laser-induced metal deposition from organometallic solution. Appl Phys Lett 44(8): 755-757.

WebElements [online], [Cited May 3, 2007], Available from: http://www.webelements.com/.

Original publications

I Kordás K, Tóth G, Remes J, Nánai L & Szatmári S (2005) Current trends in depositing and patterning metal films. In: Popescu M (ed) Optoelectronic Materials and Devices Volume 2, INOE, Romania: 239-263.

II Tóth G, Kordás K, Vähäkangas J, Uusimäki A, Leppävuori S, George TF & Nánai L (2005) Laser-induced gold deposition on p+-Si from liquid precursors: A Study on the reduction of gold ions through competing Dember and Seebeck effects. Journal of Physical Chemistry B 109(15): 6925-6928.

III Kordás K, Pap AE, Tóth G, Pudas M, Jääskeläinen J, Uusimäki A, Leppävuori S & Vähäkangas J (2006) Laser soldering of flip-chips. Optics and Lasers in Engineering 44(2): 112-121.

IV Tóth G, Kordás K, Pap AE, Vähäkangas J, Uusimäki A & Leppävuori S (2005) Origin and FEM-assisted evaluation of residual stress in thermally oxidized porous silicon. Computational Materials Science 34(2): 123-128.

V Kordás K, Tóth G, Moilanen P, Kumpumäki M, Vähäkangas J, Uusimäki A, Vajtai R & Ajayan PM (2007) Chip cooling with integrated carbon nanotube microfin architectures. Applied Physics Letters 90(12): 123105 1-3.

Book orders:
OULU UNIVERSITY PRESS
P.O. Box 8200, FI-90014
University of Oulu, Finland

Distributed by
OULU UNIVERSITY LIBRARY
P.O. Box 7500, FI-90014
University of Oulu, Finland

UNIVERSITY OF OULU P.O. Box 7500 FI-90014 UNIVERSITY OF OULU FINLAND

ACTA UNIVERSITATIS OULUENSIS

ISBN 978-951-42-8470-0 (Paperback)
ISBN 978-951-42-8471-7 (PDF)
ISSN 0355-3213 (Print)
ISSN 1796-2226 (Online)